ETHZ-IPP RP-2006-06
August 2006

Implementation of a Trigger for the Decay b → eX on the Third Trigger Level at the H1 Experiment

Lea Caminada

Diploma Thesis

supervised by
Prof. Dr. R. Eichler

Tutor: Dr. A. Schöning

Institute for Particle Physics
ETH Zürich

August 2006

Abstract

In this diploma thesis the development of a trigger for the semileptonic decay of b-quarks into electrons is presented. The trigger is implemented on the third trigger level (L3) of the H1 detector at HERA and uses the information of the Fast Track Trigger (FTT) and the new calorimeter trigger, the Jet Trigger.
The potential of different L3 electron trigger setups is studied by calculating the efficiency in simulated data and estimating the rejection power in photoproduction events.
A proposal for a future trigger strategy is derived that provides the running of a single electron trigger (with a momentum acceptance down to 2 GeV) complemented for lower momenta (> 1 GeV) by a double electron trigger. The trigger efficiency reaches $\sim$60%, whilst L3 output rates of 1-2 Hz are possible.

Kurzfassung

In dieser Diplomarbeit wird die Entwicklung eines Triggers für den semileptonischen Zerfall von b-Quarks in Elektronen vorgestellt. Der Trigger wird auf der dritten Triggerstufe des H1 Detektors bei HERA implementiert und verwendet die Daten des schnellen Spurtriggers (FTT) und des neuen Kalorimetertriggers, des Jet Triggers.
Das Potential von verschiedenen L3 Elektrontrigger Konfigurationen wird untersucht. Dazu wird die Effizienz mit Hilfe von simulierten Daten berechnet und die Ratenreduktion in Photoproduktionsereignissen abgeschätzt.
Es wird eine zukünftige Triggerstrategie vorgeschlagen, die vorsieht, dass sowohl ein Trigger für einzelne Elektronen (mit einer Impulsakzeptanz ab 2 GeV) als auch ein Trigger für zwei Elektronen mit einer grösseren Akzeptanz zu kleineren Impulsen (> 1 GeV) aufgesetzt wird. Die Triggereffizienz erreicht $\sim$60%, während L3 Ausgangsraten von 1-2 Hz möglich sind.

Contents

1 Introduction

In this diploma thesis the implementation of a trigger sensitive to the decay of beauty-quarks into electrons (b→eX) on the third trigger level at the H1 experiment is presented.
Electrons produced in the weak decay of b-quarks have low energies of 1-4 GeV and could until now hardly be identified on trigger level. The detection of these electrons can make an important contribution to the understanding of the b-quark production at low momentum and is a sensitive test for theoretical predictions.
The H1 detector is equipped with a high resolution Fast Track Trigger system and since spring with a new calorimeter trigger, the Jet Trigger. The electron trigger presented in this thesis will combine the information of the two systems in order to select reliably tracks originating from low momentum electrons.
In the following the outline of the thesis is explained:
The motivation of this study is given in chapter 2.
In chapter 3 the important components of the HERA storage ring and the H1 experiment are introduced. The subsystems relevant for this thesis, the Jet Trigger and the Fast Track Trigger, are described in more detail.
Chapter 4 contains the information about the data used for this analysis. Furthermore, the new software for the simulation of the third trigger level is presented.
The development and the design of the L3 electron trigger is discussed in chapter 5. An overview of the information available on the third trigger level is given and the trigger concept is presented. The performance is examined by considering the efficiency and the background rejection power for simulated and for measured data. Chapter 5 is terminated with a proposal for the future trigger strategy.
In the last chapter the conclusions of this thesis are given.

2 Motivation

The H1 detector at HERA is an experiment to study high energetic electron proton interactions (so called ep-events). A main focus of the H1 experiment is on heavy flavour physics investigating the production of charm- and beauty-quarks. Depending on the square of the momentum transfer from electron to proton (virtuality Q^2), two kinematic regions are distinguished. Interactions with a small momentum transfer ($Q^2 < 1$ GeV^2) are called photoproduction events, whereas events with $Q^2 > 1$ GeV^2 are referred to as Deep Inelastic Scattering (DIS). DIS events happen less frequently as the cross section of an ep-event decreases proportional to $1/Q^4$.
The H1 detector has to cope with the high event rate of the ep-scattering processes. In order to distinguish physics signals of interest from background events an effective discrimination is needed already on trigger level. The aim of this diploma thesis is to develop a trigger which is sensitive to electrons produced in the semileptonic decay of b-quarks.
At HERA heavy quarks (i.e. b- and c-quarks) are mainly produced by boson-gluon-fusion (BGF). In leading order, this process is described by a photon (emitted by the electron) and a gluon (originating from the proton) forming a quark-antiquark pair (Fig. 1). The cross section of the BGF depends on the mass and the charge of the produced particles. The larger mass and smaller charge of the b-quark relative to the c-quark (m_b=4.75 GeV, q_b=–1/3e vs. m_c=1.5 GeV, q_c=+2/3e) leads to a suppression of b-quark production by a factor of 200.
b-quarks decay via the weak interaction into c-quarks. The intermediate $W^{\pm}$-boson produces a lepton and a neutrino in about 25% of the decays. In addition, about 25% of the subsequent charm decays also have a lepton and a neutrino in the final state (Fig. 2). The charged leptons are traceable in the detector, whilst the uncharged neutrinos escape the detector unnoticed. Leptons from b- and c-quark decays can be distinguished by their momentum distribution. Due to the higher mass of the b-quark more energy is transfered to the daughter particle on average. Furthermore, the spatial separation of the lepton and the fragmentation jet is larger than in other processes and can be determined by measuring the transverse momentum of the electron relative to the jet.
b-quark production events are used to measure the gluon structure of the proton. The measurement of these events provides a sensitive test for the theoretical predictions of perturbative Quantum Chromodynamics (pQCD). Perturbative approaches give reliable results if one of the kinematic parameter defines a hard scale. Possible scales are the virtuality Q^2, the transverse momentum of the final state or the mass of the heavy quark. The electron trigger presented in this thesis is intended to be sensitive for photoproduction events including a low momentum b-quark. In such an event the hard scale is exclusively given by the large mass of the b-quark and the validity of the perturbative approche using a massive scale can be investigated.
Measurements of the b-quark production using HERA-I data have already been performed by both the H1 and the ZEUS[1] experiment. A lot of progress has been made in the understanding of the b-quark cross section in DIS and photoproduction [1], [2]-[7]. The result of these measurements are shown in Fig. 3. Plotted is the measured b-quark cross section as function of Q^2 relative to the predictions of pQCD. A slight overshoot of the measurement compared to the theoretical predictions is observable, however not yet really statistically significant.
Therefore, there is a great interest to verify these results involving more statistics.
The significantly higher luminosity after the upgrade of the HERA accelerator and the new Fast Track Trigger system (FTT) of the H1 detector open the possibility of further investigations. The FTT reconstructs tracks of charged particles in three dimensions with high accuracy and is able to identify selected topologies and event kinematics.

[1]ZEUS is an experiment located at the second electron-proton interaction point at HERA.

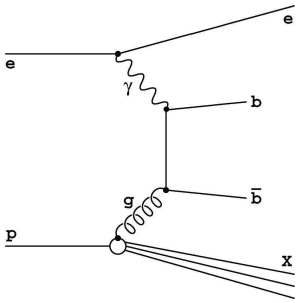

Figure 1: Leading order Feynman diagram of a boson gluon fusion process.

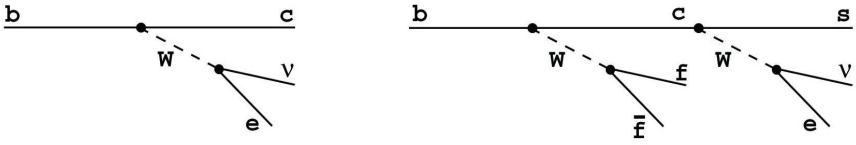

Figure 2: Feynman diagram of the semileptonic decay b→eX.

The semileptonic decay channel is very well suited for the measurement of the cross section of the production of heavy quarks because the momentum of the emitted leptons can be reconstructed in general to much more accuracy than the hadronic final state. Furthermore, the weak process involves less theoretical uncertainties and a better separation between signal (i.e. process of interest) and background.
The muonic decay channel has already been used in different measurements and is relatively easy to trigger (for $p_\perp > 2.5$ GeV) due to the clear signal of the muon in the detector.
Up to now electrons having an energy below 5 GeV cannot be triggered efficiently, because of the amount of noise in the calorimeter trigger system of the H1 detector.
However, opening a possibility to trigger these electrons might significantly increase the available statistics. In addition, the electron and muon measurements are based on signals from different components of the detector and differ in their background conditions. Therefore, the electron channel constitutes an independent measurement with its own systematics and can lead to a better understanding of the systematic errors in both measurements.
In spring 2006 the upgrade of the H1 calorimeter trigger, the so called Jet Trigger, started taking data. The new system works with fine granularity and is more sensitive to low energy depositions arising for example from low energetic electrons.
The trigger presented in this diploma thesis is intended to make best use of the calorimeter information and to combine it with the track measurement of the FTT. In this way a fast and accurate identification of electrons with low momentum should become possible at trigger level, opening a larger phase space.

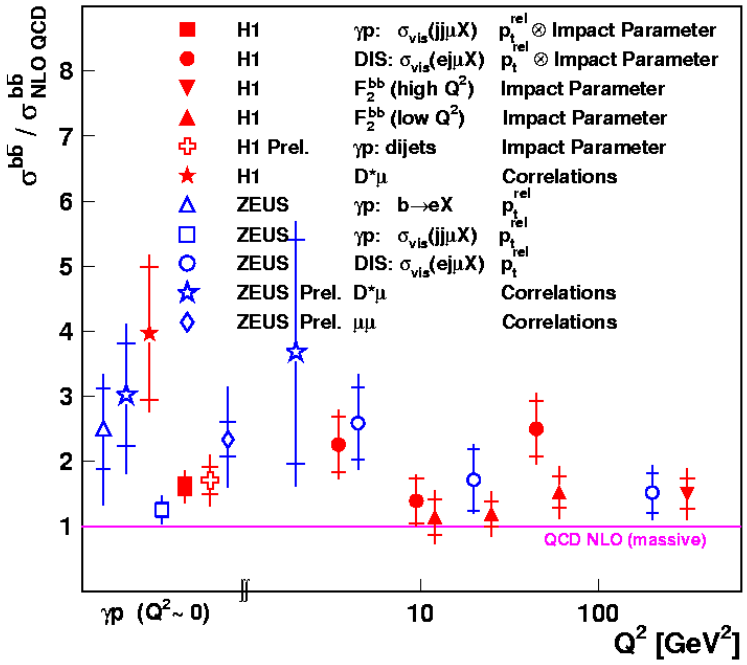

Figure 3: b-quark cross section measured by H1 and ZEUS as function of Q^2. The measurements are compared to the predictions of pQCD.

3 HERA and H1

This chapter is an introduction to the H1 experiment. It consists of a brief description of the HERA storage ring and the main components of the H1 detector followed by a more detailed view on the subsystems relevant for this thesis, namely the Jet Trigger and the Fast Track Trigger (FTT).

3.1 HERA

In the HERA storage ring high energetic protons accelerated to 920 GeV collide with electrons or positrons of 27.5 GeV. The HERA tunnel is located at DESY in Hamburg and has a length of 6.3 km. The electrons and protons are accelerated in bunches. A bunch crossing takes place every 96 ns in two interaction points where the experiments H1 and ZEUS are situated. A third experiment, HERMES, uses only the electron beam to perform fixed target experiments. A schematic view of the HERA collider is shown in Fig. 4.
HERA became operational in 1992 and its first running period (HERA-I) ended in summer 2000. In the following months a major upgrade was undertaken to achieve a five times higher luminosity. Superconducting focusing magnets were installed within H1 and ZEUS whereon the new bending of the beam forced other detector components to be adjusted. HERA-II will be operated until summer 2007.

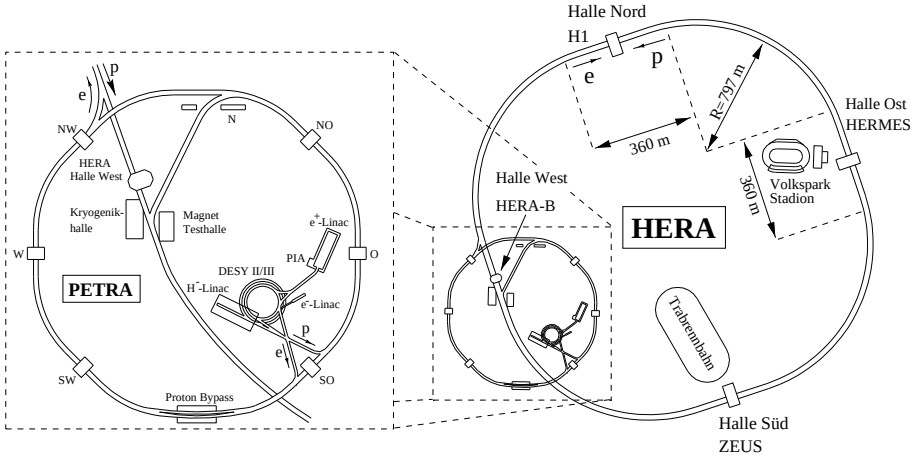

Figure 4: Schematic view of the HERA storage ring and the pre-accelerator system.

3.2 H1

The H1 detector is a general purpose detector to identify neutral and charged particles originating from the electron proton interaction in a solid angle of nearly 4π. An asymmetric instrumentational setup takes the different beam energies into account.
The tracking chambers, the calorimeter and the muon system form the main modules of the detector and are introduced in the following. A detailed description of the H1 detector can be found in [8]. Fig. 5 shows a schematic view of the H1 detector.
The H1 coordinate system is orientated such that the x-axis points to the center of the HERA ring, y points upwards and the z-axis is in direction of the proton beam. The polar angle ϑ is defined in the rz-plane, the azimuthal angle φ in the xy-plane.

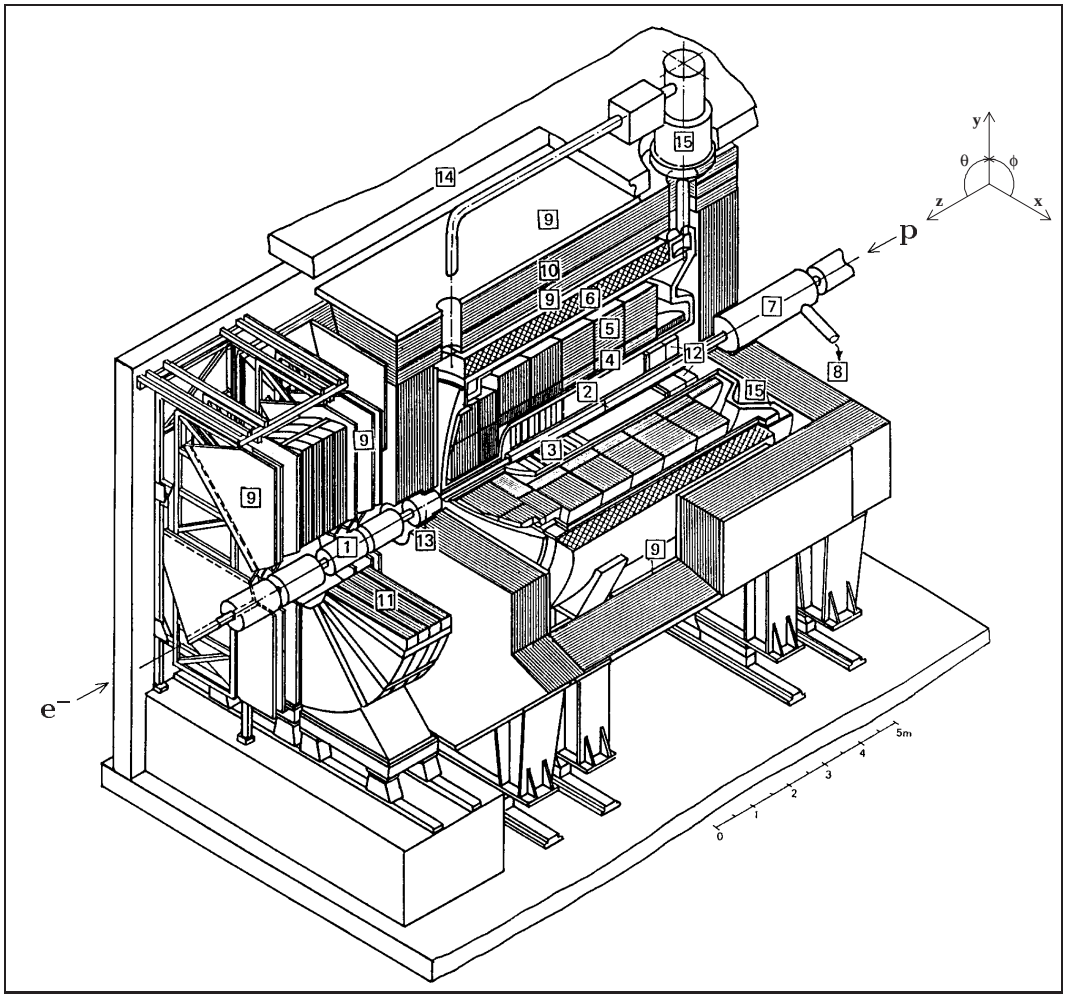

1	Beam pipe and beam magnets	9	Muon chambers
2	Central tracking device	10	Instrumented iron yoke
3	Forward tracking device	11	Forward muon toroid
4	Electromagnetic LAr calorimeter	12	Backw. electromagn. calorimeter (BEMC)
5	Hadronic LAr calorimeter	13	PLUG calorimeter
6	Superconducting coil (1.15 T)	14	Concrete shielding
7	Compensating magnet	15	Liquid argon cryostat
8	Helium supply for 7		

Figure 5: Schematic view of the H1 Detector and its subsystems.

3.2.1 Tracking Detectors

The tracking system used in the H1 detector is divided into a Central and a Forward Tracking Detector (CTD and FTD).
The Central Silicon Tracker (CST), consisting of two sensitive layers enclosing the beampipe, is the innermost detector with an angular coverage of $30\,^\circ < \vartheta < 150\,^\circ$. Two coaxial drift chambers, the Central Jet Chambers (CJC1 and CJC2), are situated outside the CST. The 24/32 layers of sense wires of the CJC1/CJC2 are strung parallel to the beam axis and form 30/60 drift cells respectively. The momentum resolution is $\sigma(p_\perp)/p_\perp \simeq 0.006 p_\perp[\mathrm{GeV}] \oplus 0.015$ in an polar angle range of $20\,^\circ < \vartheta < 160\,^\circ$. The information from the CJC is used by the FTT. The central tracking system is complemented by a multi wire proportional chamber (CIP) with high time resolution that can be used for triggering and an outer drift chamber (COZ) determining the z-position of the tracks.
In the forward region the detector is instrumented with three planar drift chambers measuring tracks in an acceptance region of $7\,^\circ < \vartheta < 25\,^\circ$.
The magnetic field of 1.14 T for the momentum measurement in the tracking chambers is produced in a superconducting solenoid surrounding the calorimeter.

3.2.2 Calorimeter

There are two main calorimeters in H1: the Spaghetti Calorimeter (SpaCal) in the backward region and the Liquid Argon (LAr) Calorimeter covering the forward and central area ($4\,^\circ < \vartheta < 155\,^\circ$).
Thin scintillating fibres placed in lead are the sensitive device of the electromagnetic and the hadronic part of the SpaCal. Due to the fine granularity in the electromagnetic sections an energy resolution of $\sigma(E)/E \simeq 0.08/\sqrt{E[\mathrm{GeV}]} \oplus 0.01$ is reached compared to $\sigma(E)/E \simeq 0.30/\sqrt{E[\mathrm{GeV}]} \oplus 0.07$ in the hadronic part. Furthermore, an excellent time resolution of about 1 ns is available. The main task of the SpaCal is the accurate measurement of the energy of the scattered beam electron.
The LAr calorimeter is a non-compensating sampling calorimeter divided in an electromagnetic and a hadronic section. Lead plates are used as absorber material in the electromagnetic part, steel plates in the hadronic part. A total of 31000 electromagnetic and 14000 hadronic readout channels lead to a resolution of $\sigma(E)/E \simeq 0.12/\sqrt{E[\mathrm{GeV}]} \oplus 0.01$ for the identification of electrons and photons and $\sigma(E)/E \simeq 0.55/\sqrt{E[\mathrm{GeV}]} \oplus 0.01$ in the hadronic case.

3.2.3 Muonsystem

Muons are identified in the massive iron yoke surrounding the H1 detector. A minimum of 1-2 GeV of energy is needed by a muon to reach the muon detector. The sensitive modules of the muon system are installed between the plates of the magnetic field returning iron yoke and provide signals for ∼100000 readout channels.

3.3 Particle Signature in the Detector

The complex design of the H1 detector allows to identify particles (if they are living long enough to reach the detector) by investigating their signature in the individual subsystems.
The electromagnetic interaction of charged particles with the filling gas (ionisation) is used in the tracking chambers to trace the signals of leptons and hadrons. Particle identification can be done by measuring the specific energy loss (dE/dx) in the CJC. Neutral particles like photons or neutrons cannot be detected in this innermost part of the detector.
Electrons and photons cause a characteristic electromagnetic shower in the calorimeter. An electromagnetic shower evolves in most cases fully in the electromagnetic section of the calorimeter and is a compact cluster.
The main interaction processes of electrons with matter are ionisation and bremsstrahlung. The amount of energy lost by bremsstrahlung is highly dependent on the material and scales linearly with the energy of the particles. For electrons with more than 100 MeV bremsstrahlung is the dominate interaction. The main part of the energy deposition within the calorimeter is caused by the emitted photons and can therefore hardly be distinguished from depositions of photons generated in the primary interaction. This separation however is already done with the help of the tracking system. The photons deposit their energy in the material (via photo effect, compton scattering and most notably pair production), inducing a second generation of electrons, positrons and photons. On average, the energy is deposited within 9/7 radiation length and the lateral size of the shower is defined by the scattering processes in the early phase.
Hadronic showers in contrast show a different shape: The shower development starts later and spreads wider in the hadronic part of the calorimeter. In addition, the hadronic radiation length is much larger than the electromagnetic radiation length. Hadrons induce a spate of inelastic interactions resulting in the generation of various secondary particles (in most cases other hadrons). Thus, the hadronic shower has a larger volume expansion and is subject to more fluctuations concerning type and number of the secondary particles. This is the main reason for the limited resolution of the hadronic energy in the calorimeter.
In a non compensating calorimeter, the fraction of the detectable energy is smaller for hadrons than for electrons. Hadrons can undergo inelastic processes involving strong interactions with nuclei. The energy used to overcome the nuclear binding energy cannot be seen in the detector. Furthermore, energy is carried away by emitted muons or neutrinos.
The difference of electromagnetic and hadronic showers diminish with decreasing energy of the particles which leads to a much more difficult particle identification in the calorimeter at low energies.
Muons generated in the event mostly have enough energy to travel through the detector causing a minimal amount of ionisation. Due to their greater mass, muons do not emit as much bremsstrahlung as electrons and are consequently able to penetrate much more matter. This penetration power is used to isolate muons behind massive iron shielding where their momentum is measured in an outer ionisation detector.

3.4 The Trigger System of the H1 Detector

In the interaction region of the H1 detector bunch crossings take place with a frequency of 10.4 MHz. The actual cross section of true ep-scattering is about 1000 Hz, the background is up to 1000 times higher. However, the read out system allows a storage of an event at a frequency of 10-20 Hz. The detector has to be equipped with a powerful trigger system selecting interesting events efficiently and at the same time reducing the background as much as possible.

The H1 trigger system is designed as a four level system (L1-L4).
The L1 system works deadtime free and provides a trigger decision within 2.3 μs. 256 trigger elements are generated by the different subsystems which investigate general properties of the event. The central trigger logically combines the 256 trigger elements to 128 subtriggers. If one of the 128 trigger conditions is fulfilled the central trigger generates a L1keep signal and the pipeline are stopped (and hence the deadtime starts). The H1 trigger strategy allows a maximum L1 output of 1 kHz. Given that some subtriggers produce higher rates their answer have to be weighted down with prescale factors.
Six of the L1 subsystems (FTT L1, Jet Trigger, Central Muon System, Forward Muon System, CIP and SpaCal Trigger) and the Central Trigger are connected to the PQZP (Parallel Quickbus Zero-suppressed Processor) system to provide their information to the L2 systems [9].
The second (L2) and the third (L3) trigger levels are enabled to open the pipelines for data taking of the next event by sending a L2reject/L3reject signal.
In case of an L1keep signal the event is revised on L2 using neural networks and topological information. In addition, an accurate measurement of the spatial position and the momentum of the tracks is performed by the second level of the FTT. The L2 decision has to be derived in 20 μs and is communicated to the central trigger in the form of 96 trigger elements. These trigger elements are used to validate the L1 subtriggers. In the case of a positive L2 decision, the detector read out starts.
The third trigger level is implemented within the FTT system and searches for specific decay channels and topologies within a latency time of 100 μs. L3 is designed to lower the L2 output rate (max. 200 Hz) at least by a factor 5.
The algorithm of the trigger presented in this thesis is performed on L3.
L4 is a software system which fully reconstructs and classifies the events. Events passing the L4 selection and a certain number of monitoring events are stored permanently. Roughly a third of the events do pass this trigger level.

3.5 The Jet Trigger

The Jet Trigger is designed to identify local energy depositions in the LAr Calorimeter within a radius of $\triangle r = \sqrt{(\triangle\eta)^2 + (\triangle\varphi)^2} \approx 0.7 - 1$, where η is the pseudo-rapidity defined as $\eta = -\ln(\tan(\frac{\vartheta}{2}))$.
The system is implemented on the first trigger level as an upgarde of the present LAr calorimeter trigger [10]. The new setup is intended to be more sensitive to low energy depositions and to provide topological information about the position of the jets in the $\vartheta\varphi$-plane using the available granularity of the LAr calorimeter to full capacity. The Jet Trigger output that is sent via the PQZP system to the FTT is a list of 16 jets sorted in energy.
The input of the Jet Trigger are the existing electromagnetic and hadronic trigger towers of the LAr calorimeter trigger [11]. A trigger tower consists of a group of LAr calorimeter cells whose granularity depends on the position in space. The typical angular coverage of a trigger tower is about 0.2 rad.
The algorithm performed by the Jet Trigger is divided into four logical stages (or units). A schematic layout of the Jet Trigger is shown in Fig. 6.
The source signals for the Jet Trigger are provided by the L1 analogue part. The signals of the LAr cells are summed and shaped (SSM: Sum and Shape Module) and thresholds are applied (AGM: Analogue Gating Modul). The BTS (Big Tower Summing) module provides on one hand the big towers for the existing LAr calorimeter trigger and on the other hand the finer granulated trigger towers which are passed to the Jet Trigger.

ADC-Calculation-Storage Unit (ACS) In a first step the input towers for the jet finding algorithm are re-assembled. The Jet Trigger system is equipped with 72 ACS cards, 9 for each octant of the calorimeter. On the ACS cards the analogue pulses from the electromagnetic and the hadronic section of the trigger towers are digitised separately. In order to make an effective noise suppression, thresholds and weights are applied before summing the signals from the electromagnetic and the hadronic part.
The mapping from the trigger towers to the input towers differs for the forward and the backward region. In the forward region the finest possible granularity of the trigger towers is preserved whereas in the backward region several trigger towers are mapped to one input tower. Due to the forward boost of the jets a higher spatial resolution is only required in the forward region. The combination of trigger towers in the backward region reduces the data to process without loosing physics information. To define the position of an input tower the ϑ-region is divided into 22 segments, the φ-region in 8, 16 or 32 segments depending on the ϑ-position. A map of the input towers is shown in Fig. 7.
The digitized energy of the weighted input towers and their address is stored on the ACS cards and transfered to the Bump Finder Unit.

Bump Finder Unit (BFU) In the BFU the search for local energy maxima is performed. Bumps are defined as the maxima of local energy deposition, including neighbouring input towers. Neighbouring towers have to be taken into account to allow the identification of energy depositions within a region of $\triangle r \approx 1$.
The basic jet finding algorithm is a parallel process carried out on four BFU cards. Every BFU card searches bump centers in two octants of the calorimeter. Thereto the energy content of each input tower is compared with its eight or nine immediate next neighbours. The energy of the bump is calculated by summing the energy of the bump center and of the nearest neighbours. The address of the bump is given by the address of the center. From the BFU a maximum of 24 jets is passed to the Sorting Units.

Primary and Secondary Sorting Unit (PSU and SSU) In the PSU the bumps found in each of the four BFU's are sorted according to their energy. In case of equality a further sorting in ϑ and φ is performed. The first 8 bumps from every card are fed into the secondary sorting unit and are sorted again according to the same criteria. The output is an ordered list of 16 jets defined by energy, ϑ and φ.
This information is sent to the L2 subsystems connected to the PQZP port as well as to the Trigger Quantity Determination Unit.

Trigger Quantity Determination (TQD) There are 16 trigger element generators receiving the list of the ordered jets and taking an independent decision. A typical action of the TQD is counting the number of jets above certain thresholds or determining the topology of an event. The applied criteria depend on the physics interest and the current background conditions and should therefore be flexible and expandable. The generated trigger elements are finally sent to the central trigger.

At the time the experimental work for this thesis was done, the LAr calorimeter was equipped with the complete Jet Trigger hardware only in the forward region ($4\,^\circ < \vartheta < 45\,^\circ$). The extension toward the central barrel ($45\,^\circ < \vartheta < 155\,^\circ$) was commissioned in July and August.

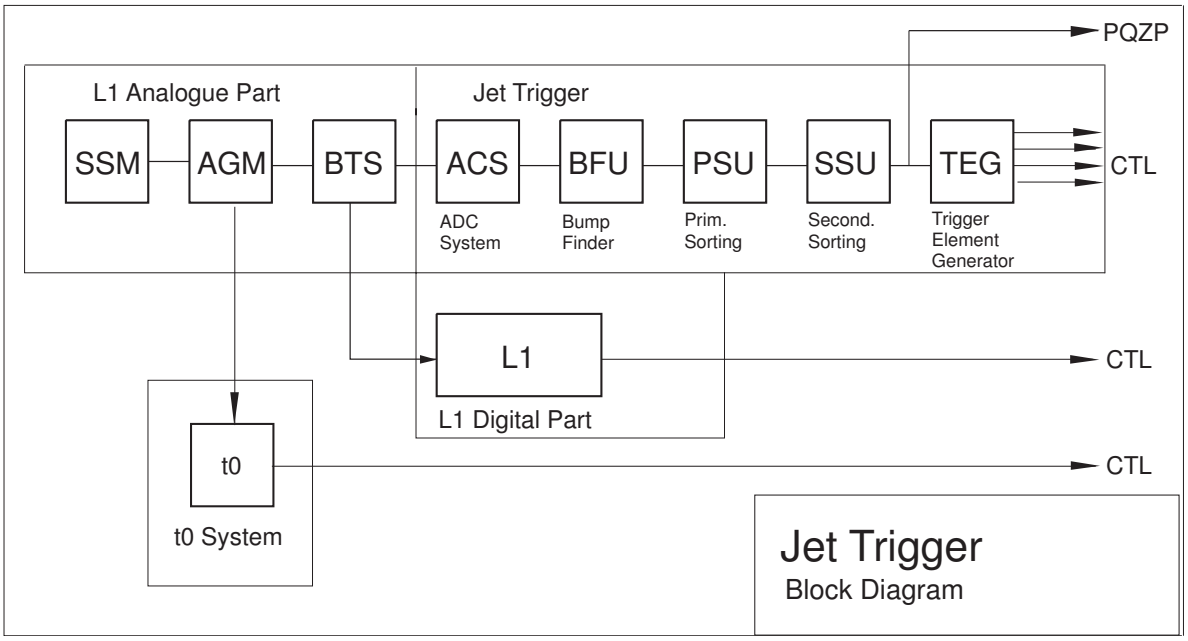

Figure 6: Schematic layout of the Jet Trigger.

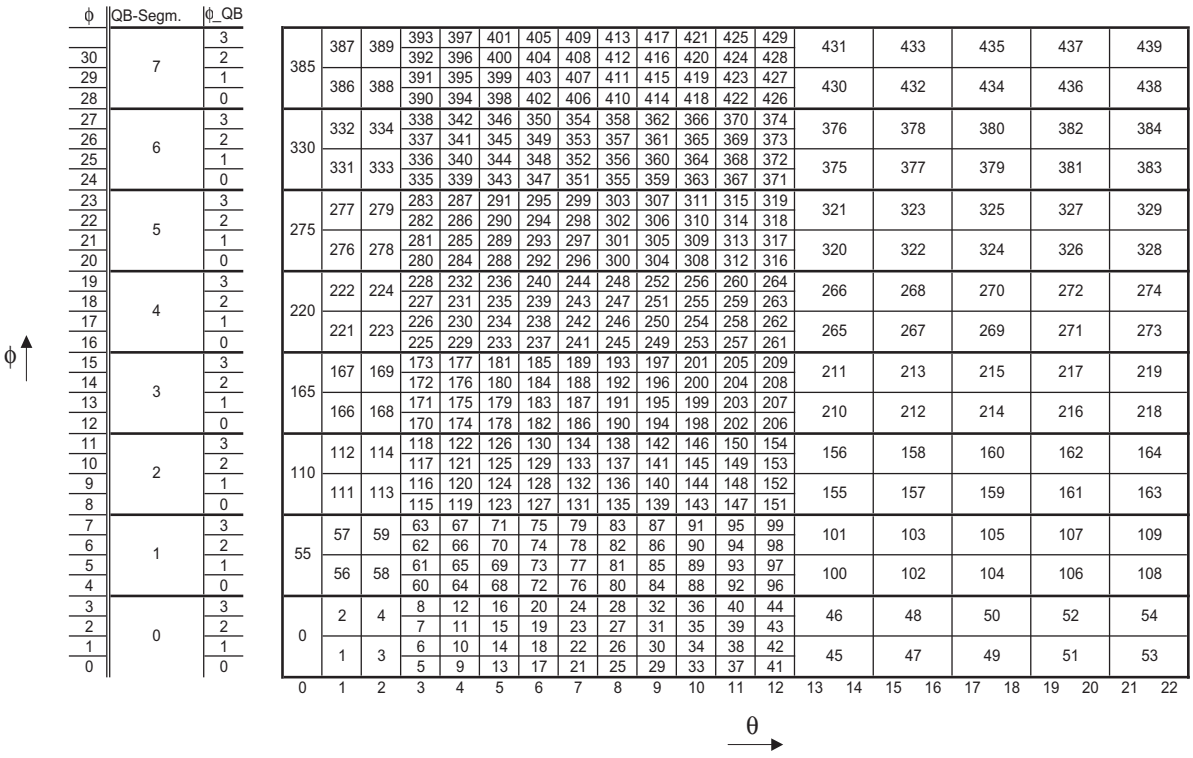

Figure 7: Summed Input Towers of the Jet Trigger (Hardware Address).

3.6 The Fast Track Trigger

The Fast Track Trigger (FTT) was one of the upgrade projects of the H1 experiment for the HERA-II running period [12]. The aim is to perform an efficient and fast identification of tracks in the central region of the detector ($20\,^\circ < \vartheta < 160\,^\circ$) with a transverse momentum $p_\perp > 100$ MeV. The new design of the programmable logic chips allows the system to cope with the significantly higher background rates compared to the HERA-I running period.
The FTT is embedded in the first three trigger levels of H1. The schematic layout of the technical implementation is shown in Fig. 8.
To determine the track parameters, the FTT uses the analogue signals from selected wires of the CJC, three trigger layers in the CJC1 and one in the CJC2. A trigger layer consists of three layers of wires at a defined radial distance within the tracking chamber. The group of three wires in the same CJC cell together with two wires of the neighbouring cells is called a trigger group. Fig. 9 shows a rφ-view of the CJC where the wires used by the FTT are marked.

L1 On the first trigger level a search for hits and track segments in each of the four trigger layers is performed independently, followed by a rough track linking of these segments in the rφ-plane.
The analogue CJC information is digitised on both ends of the 450 selected wires via Fast Analogue Digital Converter cards (FADC). The FADCs are integrated on 30 Front End Modules (FEM) which process the signals from five trigger groups each. A Qt-algorithm [14] is implemented to determine the charge Q deposited on a wire and the time t at which the hit is measured. This is done using the so called difference of sample (DOS) technique. The z-information is obtained with the charge division method. The result of the Qt-algorithm is fed into an 80 MHz shift register. To reduce the input data for L1 a 20 MHz shift register is filled in parallel. In addition the z-information is stored in a 20 MHz shift register. The resulting pattern in the shift registers are compared to pre-calculated patterns originating from validated tracks. Content Addressable Memories (CAM) allow an effective and fast pattern recognition: The input to a CAM are precalculated validated pattern, whilst the output are the parameters κ (curvature) and φ (angle at vertex position) of the associated track segment.
The track segments are filled in a κ-φ histogram and sent from the FEMs via the merger cards to the L1 Linker Card. On the Linker Card the histograms are combined and a sliding window technique is applied to look for similar κ-φ values of segments in different layers. Tracks are identified if at least two segments from different layers can be combined. On the basis of these tracks up to 32 trigger elements for the central trigger can be generated. The finding process has to be finished after 1.9 μs before the L1 trigger decision is sent to the central trigger.

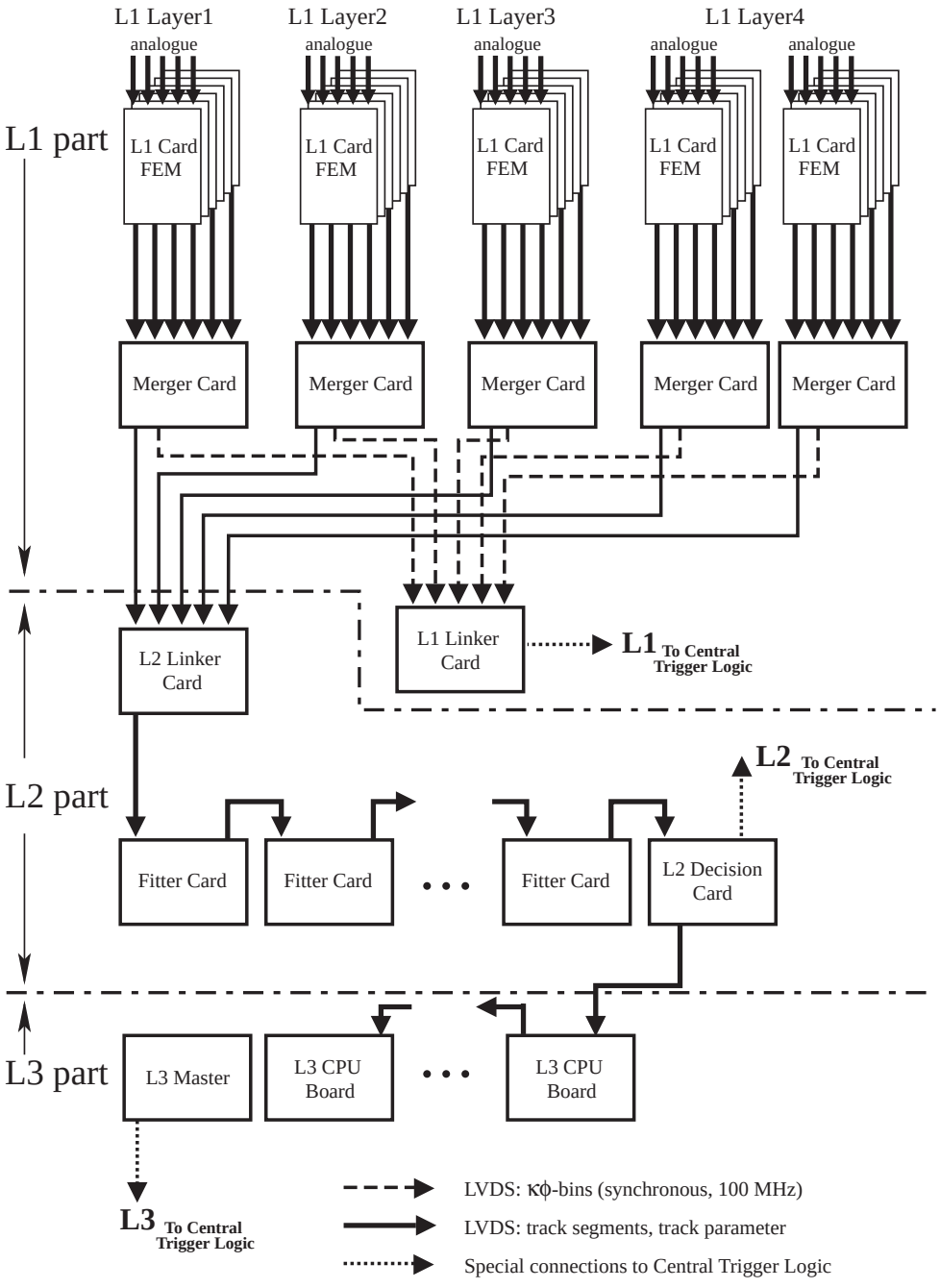

Figure 8: Schematic layout of the FTT hardware.

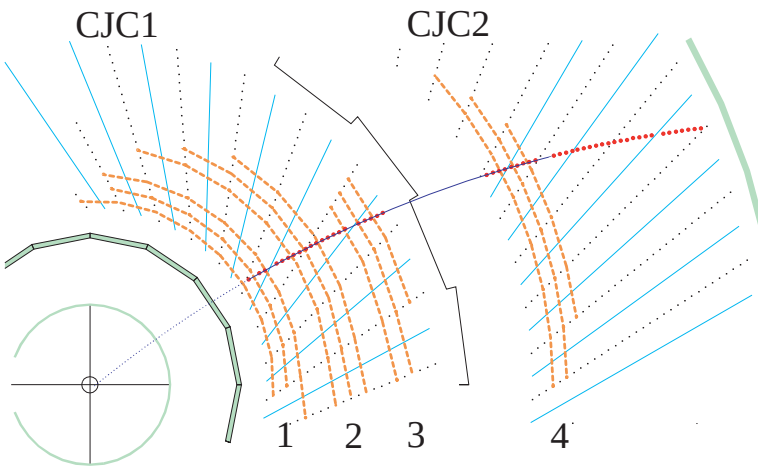

Figure 9: Trigger layers in the CJC used by the FTT.

L2 A more accurate segment finding and a linking in three dimensions is done on L2 where 20 μs of latency time can be used to run the algorithm. The output is up to 48 tracks with a resolution comparable to the full offline event reconstruction.
If the central trigger takes a positive L1 decision, the second level of the FTT is activated. The track segments found on the previous level are validated again, this time exploiting the full resolution of the 80 MHz shift register. The result is transferred to the L2 Linker Card, where the two dimensional track finding is performed using the same criteria as on L1. The track parameters κ and φ of a revised track are sent together with the z-information to one of the six fitter cards.
On the fitter cards the track parameters are fitted in the rφ-plane using a primary vertex constraint. Subsequently a second fit in the rz-plane is performed. The result is a maximum of 48 three dimensional tracks characterised by the five parameters $p_\perp$ (transverse momentum), d_{ca} (distance of closest approach to the origin), φ, ϑ and z_0 (z-coordinate of the track at the point of closest approach).
The track information is sent to the L2 decider card where the L2 trigger decision is taken. In addition, the L2 decider card receives the information from the other subsystems via the PQZP port.

L3 In case of a L2keep signal from the central trigger the information on the L2 decider card is forwarded to the L3 system. The L3 system consists of a farm of PowerPC cards (CPU cards) which are used to perform further analyses of the event on the basis of the FTT L2 track data and additional information from other subdetectors sent via the PQZP system. 100 μs are available to derive a L3 decision. Each CPU card runs a specific algorithm to extract exclusive final states. The setup is configured to manage up to 16 CPUs cards, 4 of which are currently installed and running. The L3 system works with a real time operating system and allows the implementation of code written in the high level programming language C.
A detailed description of the L3 system can be found in [15], [16], [17]. The schematic setup of L3 is shown in Fig. 10.

The L3 receiver card gets the data from the L2 system and distributes the information to the CPU cards. The so called FPDP (Front Panel Data Port) connection allows a parallel data transfer. Thus, the finding algorithms on each CPU card can start simultaneously. The different L3 finding algorithms work in parallel and take independent trigger decisions. In the case of a positive decision a trigger bit is set on the trigger bit card. The triggerbit card sends the decision to the central trigger.
In order to allow a quick data processing all cards are integrated in a VME Crate (a case for electronic cards meeting the Versa Module Eurocard Standard) which provides a common interface. The L3 Master card, also installed in the VME crate, reads the information from the receiver card and the four CPU cards and writes it to the H1 database.
The present setup of the L3 trigger elements generated by the different finder is listed in Appendix A.

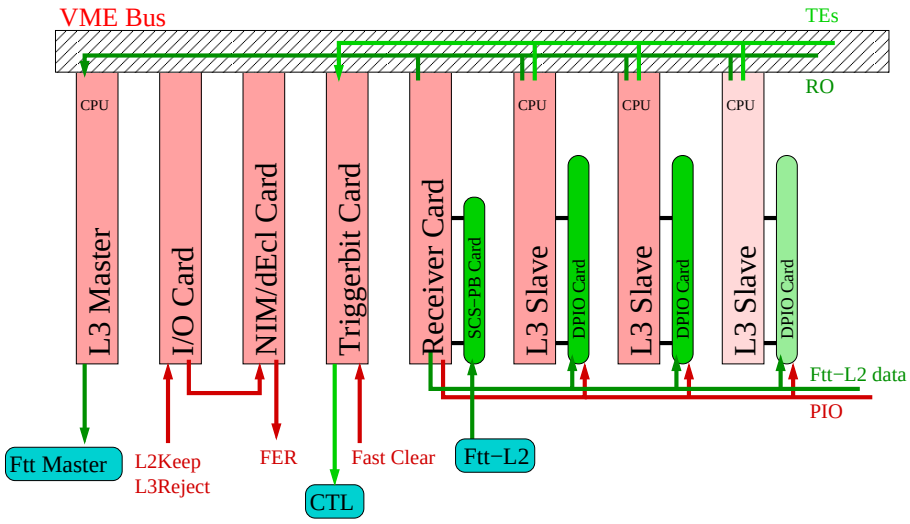

Figure 10: Schematic layout of the FTT L3 system.

4 Data and Simulation

In this chapter an overview of the data used in this study and the L3 trigger simulation is given. A short introduction to the H1 data storage system is followed by a description of the data and a detailed discussion of the L3 simulation software.

4.1 Data Storage at the H1 Experiment

The data storage system of the H1 experiment is now introduced briefly. The H1 experiment uses the so called BOS[2] bank system which allows a well structured data storage [18]. A BOS bank has a four letter long name and a defined format usually consisting of 16 or 32 bit data words.
For every event the data is filled into BOS banks, generated separately by each subsystem. The full detector reconstruction is performed on this data and creates additional BOS banks to store the output.
The detector simulation uses the same data format. A Monte Carlo (MC) simulation of the H1 experiment can be subdivided into three independent steps. The generation of a physical event is followed by a simulation of the detector response and the reconstruction of the data using the same software as for measured data.
The result of the detector simulation is again written to BOS banks and can consequently be accessed in the same way as the data from the real experiment. The BOS banks created by the simulation software have usually the same name as the ones generated in a real event.

4.2 Data Sets

The data used in this analysis was taken in June 2006 in the H1 data taking runs 465525-466829. A sample of 200000 events triggered by the L1 subtriggers 53, 56 and 120 and a sample of 140000 events triggered by the subtrigger 61 are selected from this run period. Only runs with the FTT and the Jet Trigger in the read out are taken into account for this study.
The L1 and L2 trigger conditions of the subtriggers 53, 56 and 120 are listed in appendix C. Furthermore, two MC simulations produced by the generator PYTHIA [19] are used for this analysis. The details can be found in Table 1.

Generator	Physics	Cuts
PYTHIA 61	Open b-Quark Production	$p_{\perp electron} > 1.5$ GeV, $p_{\perp jet} > 4$ GeV
PYTHIA 62	Minimum Bias Photoproduction	$p_{\perp track} > 1.9$ GeV, $p_{\perp jet} > 4$ GeV

Table 1: MC simulations used in this study.

[2]Bank Object System

4.3 L3 Trigger Simulation

The input for the L3 simulation is data either measured in the experiment or generated in a Monte Carlo simulation which allows on one hand to estimate the physics potential of the trigger and on the other hand to verify the performance of the hardware implementation. The L3 simulation is written in the programming language C and is largely identical to the software implemented in the hardware. The L3 code is implemented within the simulation package of the FTT (FTTEMU4). In order to provide a serviceable working environment also the Jet Trigger simulation is integrated in FTTEMU4.

4.3.1 Data Processing in the L3 Hardware

In the following the data processing in the hardware implementation of the L3 system is described. The simulation software is designed to follow this procedure as closely as possible. Each of the different L3 finding algorithms is running on one of the four CPU cards. The input data to the L3 system is collected on the L3 receiver card, from where it is simultaneously delivered to the memories of the different CPU cards. The L3 master card reads the data from the memory of the L3 receiver card and creates the BOS bank TT3R which contains the L2 track parameters and the PQZP information. In order to controll the data flow between the receiver card and the CPU cards, the memory of each CPU card is read out and written to the TT3T bank which is created with different version numbers corresponding to the CPU cards.
In a final step the L3 master card collects the trigger decisions of the different finding algorithms and stores the information in the TT30 bank.
Fig. 11 shows the data processing in the hardware schematically.

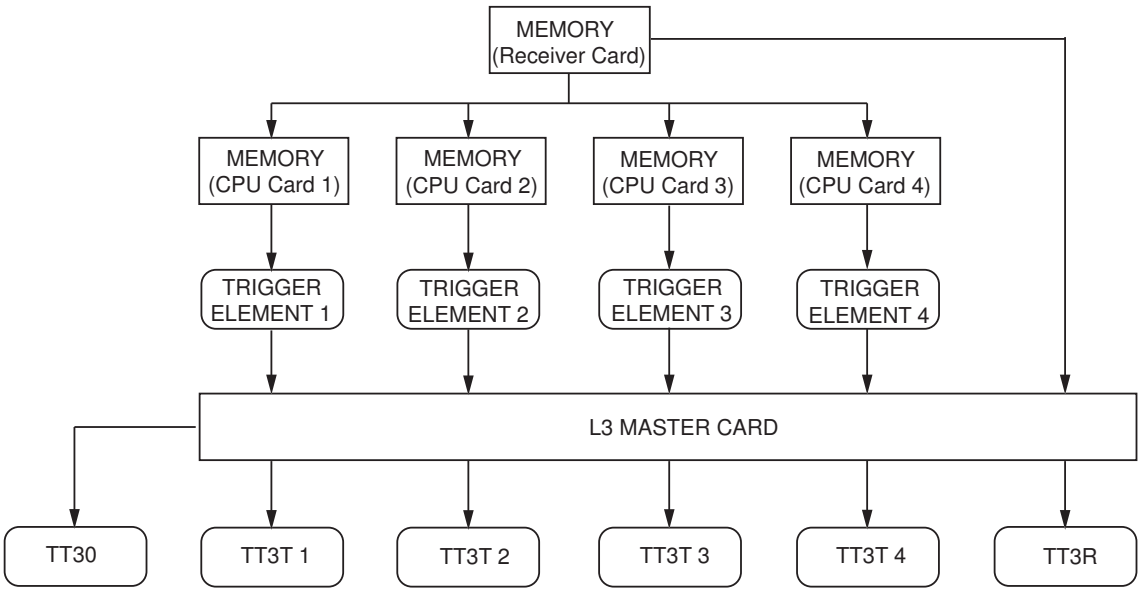

Figure 11: Data processing in hardware.

4.3.2 Data Format of L3 Input

The input data to the L3 system is on one hand the track parameters determined by the first two levels of the FTT and on the other hand the Jet Trigger information received via the PQZP system.
The Jet Trigger information is encoded in 16 32-bit words. Every jet is described by its energy and the $\vartheta\varphi$-position corresponding to the input tower map (compare Fig. 7). The second level of the FTT transmits data clusters (3 32 bit words) of up to 48 fitted tracks. A track is characterized by the following three parameters: the inverse transverse momentum of the track $1/p_\perp$, the polar and the azimuthal angle in form of cot ϑ and $\varphi^* \simeq \frac{4}{\pi}\varphi$ [13].
The bit pattern of the Jet Trigger and FTT data is shown in Table 2 and 3.

31...29	28...24	23...21	20...16	15...8	7...0
000	ϑ	000	φ	00000000	E

Table 2: Bit pattern of a data word of the Jet Trigger.

31...0
$1/p_\perp$ (float)
cot ϑ (float)
φ^* (float)

Table 3: Bit pattern of the data words of the FTT.

4.3.3 Simulation and Verification of the L3 Performance

FTTEMU4 is the emulation software of the FTT [13]. FTTEMU4 has a modular design which allows to describe virtually all features of the FTT hardware implementation. It starts with the hit finding on the basis of the CJC information and reproduces successively all the steps of the FTT track finding algorithm. The L3 simulation software forms a separate module within the FTTEMU4 program package. The PQZP branch containing the Jet Trigger information is provided by the Jet Trigger Simulation. The information of the LAr trigger towers supplies the input data for the Jet Trigger simulation. The four stages described in chapter 3.5 are then simulated in order to emulate the Jet Trigger performance.
The FTT and the Jet Trigger simulation programs can be run on data from real events as well as on data generated in a MC simulation. For the purpose of this study an interface routine is written that allows to implement the Jet Trigger simulation into FTTEMU4.
In a MC simulation the input data for the L3 finding algorithm has to be generated. This is done by the simulation of the first two FTT levels and the Jet Trigger delivering the data in the same bit format as in the hardware implementation.
The processing of this data and the filling of a memory similar to the one on the CPU cards is subject to the L3 software. The 32-bit BOS bank TT3R is created to store the FTT L2 track parameters and the data received via the PQZP system. From the TT3R bank the data is subsequently transfered to the memory where it can be accessed by the L3 program code. The trigger decision taken in the simulation software is written to the TT30 bank.
The implementation of the L3 finding algorithm is very similar in the online code and the simulation. The memory accessing is different because of the differing hardware environment. However, the same C-routines are used for the actual finding algorithm.

In order to verify the performance of the hardware implementation the L3 simulation software can be processed on measured data. In this case the content of the TT3R bank written online during data taking is used as input. This data is again written to the memory and the L3 simulation program proceeds as described before. The trigger elements generated in this process are then compared to the online decisions. A consistent result confirms the reliability of the hardware implementation.
The process sequence of the L3 simulation software is displayed in the diagram in Fig. 12.

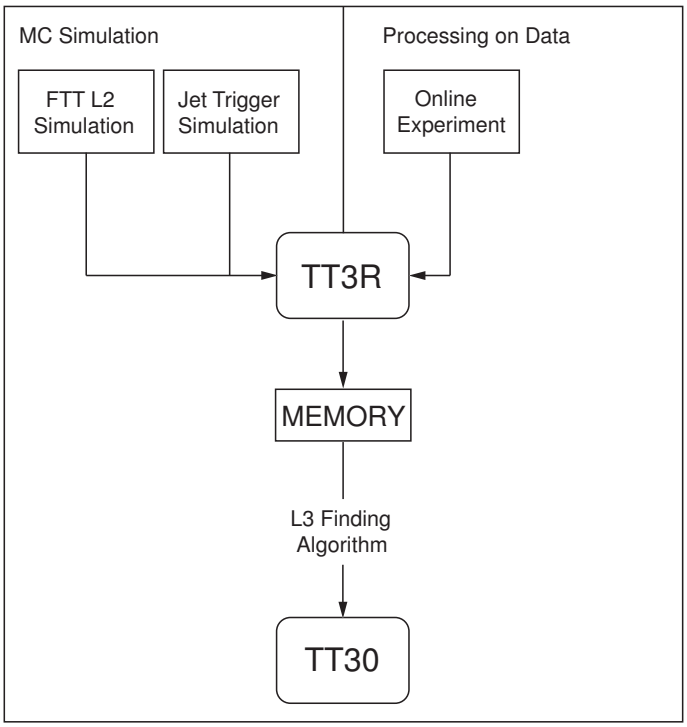

Figure 12: Processing of the L3 simulation software on simulated and measured data.

5 The L3 Electron Trigger

The development and the design of an L3 trigger is presented in this chapter.
The L3 electron trigger is intended to allow an efficient identification of electrons from b-quark decays having energies of about 1-4 GeV. At the same time the trigger should reject background events effectively. The aim is to achieve a L4 input rate of about 1-2 Hz. A trigger setup which best meets the competing demand of highest efficiency and maximum signal to background rejection has to be developed.
In the first part the input of the L3 electron trigger and the data selected for this study will be described. The trigger concept is introduced in the following.
An appropriate L3 electron trigger setup is derived on the basis of MC simulations of b-quark production events. The design of the trigger is implemented and revised by evaluating the performance in measured data. The signal to background rejection power is estimated on the basis of photoproduction events.
The results are discussed in order to derive a proposal for an optimum trigger strategy.
In the last section the current implementation of the L3 electron trigger in the FTT hardware is presented.

5.1 Input of the L3 Electron Trigger

The L3 electron trigger uses the FTT L2 and Jet Trigger information as input. The raw data of the two triggers is preprocessed before performing the actual L3 finding algorithm. The data is delivered in the same format in the hardware implementation as in the simulation.
The track parameters $1/p_\perp$, $cot\ \vartheta$ and φ^* available from the FTT are converted to $p_{\perp FTT}$, $\vartheta_{FTT} \in [0, \pi[$ and $\varphi_{FTT} \in [0, 2\pi[$. The tracks measured by the FTT are restricted in the forward region by the acceptance of the CJC ($\vartheta > 0.3$ rad).
The energy information of the Jet Trigger is encoded in a maximum of 256 counts (8 bit) where one count corresponds to ∼100 MeV in measured data and to ∼125 MeV in a MC simulation. The transverse energy of a jet is obtained by $E_{\perp JT}[\mathrm{GeV}] = \frac{\mathrm{E[counts]}}{10(8)} \sin\vartheta$ for data and simulation, respectively. The φ and ϑ integer value measured by the Jet Trigger designate the position of the input towers and are translated to $\vartheta_{JT} \in [0, \pi[$ and $\varphi_{JT} \in [0, 2\pi[$ using a lookup table containing the encoded geometry [20]. However, with the Jet Trigger not being fully installed, the Jet Trigger acceptance region is restricted to $\vartheta_{JT} < 1$ rad. Therefore, the L3 electron trigger has currently an acceptance region of about 0.7 rad determined by the narrow overlap of the Jet Trigger and the CJC.

5.2 Data Selection

Three data samples were used in this study: a sample of photoproduction events triggered by the L1 subtriggers 53, 56 or 120 and two sets of MC simulated events, one describing b-quark production the other minimum bias photoproduction.
On the basis of the b-quark MC simulation the optimum design of the L3 electron trigger is determined and the efficiency in the simulation is calculated.
Since no sample of preselected b-quark events was available, the performance of the L3 electron trigger in data is investigated using a set of events triggered by the high multiplicity photoproduction subtriggers 53, 56 or 120. These subtriggers have all the same L1 condition asking for a high multiplicity event in the central region of the detector and differ on L2 in the requirements on the event topology. Similar trigger conditions on the first two trigger levels are intended to be applied in the L3 electron trigger setup.

The L1 and L2 conditions of the subtriggers 53, 56 and 120 are listed in Table 4.
The minimum bias photoproduction MC sample provides the link between data and simulation. The kinematics of the generated events is close to the one in the selected data sample. In contrast to the data sample, a trigger selection is not performed in the MC simulation.
A comparison between the FTT and Jet Trigger response in data and simulation (photoproduction MC) is shown in Fig. 13 and 14.
The correlation in the transverse momentum distribution of the FTT is satisfactory. The dashed line shows the $p_\perp$-distribution of electrons from b-quark decays obtained in a MC simulation and indicates the region of interest. In the b-quark MC the electrons are generated having a minimum $p_\perp > 1.5$ GeV. The major differences between the photoproduction data and simulation arise at low values of $p_\perp$ outside the momentum acceptance region. A small raise can be observed in the photoproduction MC simulation at $p_\perp > 1.9$ GeV which is caused by a cut on generator level at this value.
The φ-distribution of the FTT shows a dip in the region of 2 rad $< \varphi <$ 4 rad that is more distinct in data than in the simulation. This effect is caused by hardware problems within the CJC. The ϑ-distributions in data and simulation agree well and show a larger amount of tracks reconstructed in the forward and the backward region.
The performance of the Jet Trigger shows major differences in data and simulation. The discrepancy in the Jet Trigger response is most significant in the φ-distribution and is an indication of hardware or calibration problems.

Subtrigger	L1 condition	L2 condition
53	> 5 tracks with $p_{\perp FTT} > 100$ MeV && > 2 tracks with $p_{\perp FTT} > 400$ MeV && > 1 tracks with $p_{\perp FTT} > 900$ MeV && > 0 tracks with $p_{\perp FTT} > 1800$ MeV&& CIP significance > 2 && > 10 entries in CIP histogram	$\Sigma\, p_{\perp FTT} > 6.5$ GeV && ≥ 2 tracks with $p_{\perp FTT} > 800$ MeV
56		Neuronal Net for untagged D* && $\Sigma\, p_{\perp FTT} > 6.5$ GeV && FTT L2 z-vertex condition
120		Neuronal Net for untagged D* && FTT L2 z-vertex condition && ≥ 2 tracks with $p_{\perp FTT} > 800$ MeV

Table 4: L1 and L2 conditions of the subtriggers 53, 56 and 120.

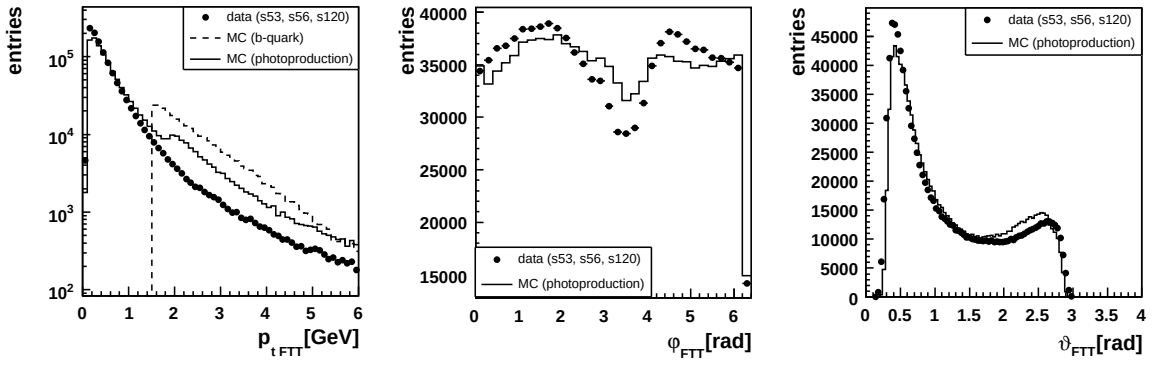

Figure 13: $p_{\perp_{FTT}}$-, φ_{FTT}- and ϑ_{FTT}-distribution of tracks measured by the FTT. The points represent a data sample triggered by the subtrigger 53, 56 or 120, the solid line a photoproduction MC simulation. The dashed line shows the momentum distribution of the electrons generated in the b-quark MC simulation. The distributions are normalised.

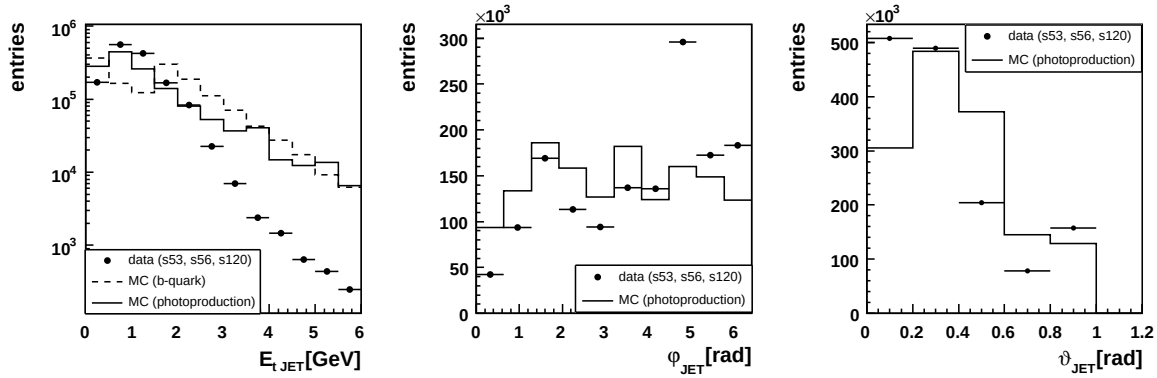

Figure 14: $E_{\perp_{JT}}$-, φ_{JT}- and ϑ_{JT}-distribution of jets measured by the Jet Trigger. The points represent a data sample triggered by the subtrigger 53, 56 or 120, the solid line a photoproduction MC simulation. The dashed line shows the momentum distribution of the electrons generated in the b-quark MC simulation. The distributions are normalised.

5.3 Concept of the Trigger

The concept of the L3 electron trigger is based on the idea of matching the track data of the FTT to the energy measurement of the Jet Trigger. Both systems together provide information about a particle's momentum, its energy and the position in the $\vartheta\varphi$-plane that has to be combined in an adequate way.
In a first step the clusters of energy deposition in the calorimeter are matched with tracks taking advantage of their spatial correlation. To assure that the electron reaches the calorimeter without being deflected by the magnetic field in the tracking chambers a minimum transverse momentum $p_{\perp_{FTT}} > 1$ GeV is required. The momentum distribution shown in Fig. 13 indicates that this requirement reduces the input rate for the L3 finding algorithm considerably. The track cluster matching is done by allocating to every FTT track a Jet Trigger cluster in

the calorimeter. Cluster within an acceptance window around the track's impact point are selected. The size of the acceptance window is determined by the choice of two parameters:

$$\Delta\varphi = \varphi_{FTT} - \varphi_{JT} \text{ and } \Delta\vartheta = \vartheta_{\mathrm{FTT}} - \vartheta_{\mathrm{JT}}.$$

The optimum value of these parameters is analysed in detail later on.
An accurate track-cluster matching allows to reject tracks which have been wrongly reconstructed by the FTT. The relative fraction of fake track increases with the momentum of the track. Therefore, the L3 electron trigger is expected to have a high rejection power most notably for high $p_\perp$ tracks.
For the purpose of particle identification already on trigger level the energy and momentum measurements are correlated. The main focus is on discriminating electrons and high energy pions. As discussed in section 3.3, the amount of energy detectable within the calorimeter is smaller for hadrons than for electrons. Almost the whole electron energy is observable in the calorimeter in contrast to only 40-80% of the hadronic energy. Therefore, the ratio $E_\perp/p_\perp$ (transverse energy measured by the Jet Trigger divided by the FTT-track's transverse momentum) is expected to show a clear maximum at 1 in the electron case, whereas a major part of the hadrons will have a ratio of $E_\perp/p_\perp < 1$ leading to a visible lower tail in the distribution. The introduction of a minimum threshold in the $E_\perp/p_\perp$-distribution should consequently permit a coarse distinction of electrons and hadrons.
A set of events selected by the subtriggers 53, 56 or 120 is used to perform the matching of the FTT tracks and the energy cluster detected by the Jet Trigger. FTT tracks with a transverse momentum of $p_{\perp_{FTT}} > 1$ GeV lying in the spatial acceptance region of $\vartheta < 1$ rad and Jet Trigger clusters with energy $E_{JT} > 10$ counts ($\sim$ 1 GeV) are taken into account. The spatial correlation of the FTT tracks and the Jet Trigger clusters in data is shown in the first two plots in Fig. 15. The $\Delta\varphi$- and $\Delta\vartheta$-histograms displayed show a maximum at the expected position at 0. The FTT resolution in φ ($\sim$0.003 rad) is much more accurate than the Jet Trigger resolution ($\sim$0.1-0.4 rad). This leads to the plateau in the φ-distribution. In contrast, the gaussian like ϑ-distribution confirms that the ϑ-resolution of the FTT and the Jet Trigger are comparable (FTT: $\sim$0.075 rad, Jet Trigger: $\sim$0.1-0.2 rad).
The third plot in Fig. 15 shows the $E_\perp/p_\perp$-distribution of matched track cluster pairs. Loose cuts in $\Delta\varphi$=0.4 rad and $\Delta\vartheta$=0.3 rad are applied. The distribution shows a wide maximum near one descending to a tail at small values. These signals are suppressed by applying a lower $E_\perp/p_\perp$ cut. An upper $E_\perp/p_\perp$-cut is not introduced as it is not expected to have a significant effect on the signal to background reduction. Furthermore, non isolated electrons could be lost by an upper cut. A neighbouring photon or hadron could increase the amount of energy measured in a Jet Trigger cluster and cause a higher $E_\perp/p_\perp$-value.

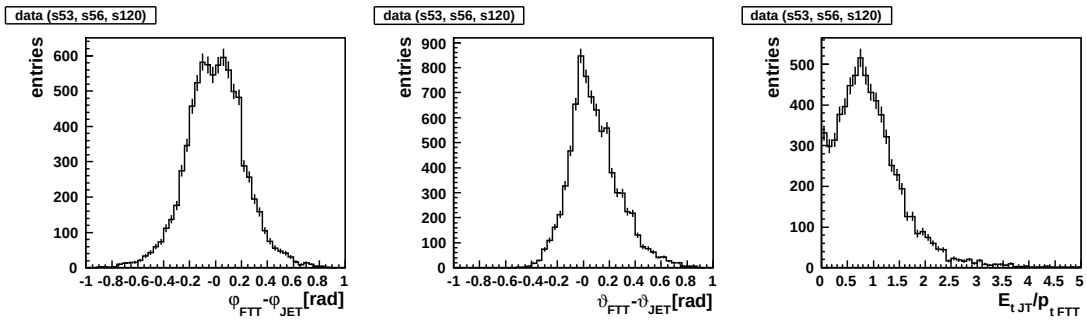

Figure 15: Spatial correlation of the FTT tracks and Jet Trigger clusters ($\Delta\varphi$- and $\Delta\vartheta$-histogram) and $E_\perp/p_\perp$-distribution obtained by the FTT-Jet Trigger-matching in data.

5.4 Monte Carlo Study to optimise the Design of the Trigger

Monte Carlo studies are performed to determine the potential of the L3 electron trigger by estimating its efficiency using simulated events.
Within the scope of this analysis a set of 50000 MC events simulating the semileptonic decay of b-quarks into one or more electrons was used.

5.4.1 Selection of the Generated Electrons

Electrons of the decay channels of interest (b→eX and b→cX→eX') are identified by looking at the generated information.
The link to this information is accessible in the DTNV bank which stores the parameters of non vertex fitted tracks reconstructed within the central and the forward tracking chambers. Every DTNV track points to the corresponding simulated particle in the STR bank. A further link from the STR to the GTR bank provides the generated information. The procedure of tracing back the particle relations is described in the diagram displayed in Fig. 16.
Only generated electrons which are found in the reconstruction originating from the primary vertex are taken into account. The fit hypothesis of a DTNV track is available in the DTRA bank which stores the parameters of the vertex fitted tracks. The use of these parameters is preferred in this study due to their higher accuracy.
In order to determine the FTT response caused by the generated electrons, the FTT tracks have to be related to the tracks found in the reconstruction. To every FTT track the closest reconstructed DTRA track is assigned. The measure for the distance between FTT and DTRA tracks is defined by

$$R^2 = \left(\frac{\frac{1}{p_{\perp_{FTT}}} - \frac{1}{p_{\perp_{DTRA}}}}{0.03} \right)^2 + \left(\frac{\varphi_{FTT} - \varphi_{DTRA}}{0.003} \right)^2 + \left(\frac{\vartheta_{FTT} - \vartheta_{DTRA}}{0.1} \right)^2 .$$

The denominators weight the difference of the track parameters according to the FTT resolution.
The FTT track inherits the link to the simulated particle (and hence to the generated particle) from the reconstructed track assigned.

5.4.2 Input Generated by the b-Quark MC Simulation

The reconstructed $p_\perp$-, φ- and ϑ-distributions (DTRA) of the generated electrons are displayed in Fig. 17. In the first plot also the generated transverse momentum distribution can be seen (dashed line). In the b-quark MC simulation applied for this study the events are generated with at least one electron having a transverse momentum of $p_{\perp_{GTR}} > 1.5$ GeV. This cut leads to the sharp increase of the $p_\perp$-distribution above the threshold. The electrons with lower transverse momentum arise from other decays and can hardly be seen by the L3 electron trigger. The $p_{\perp_{DTRA}}$-distribution obtained by the reconstruction is shifted to lower values due to bremsstrahlung losses of the electrons within the detector. The flatness of the φ-histogram confirms the isotropy of the decay in the plane transverse to the beam direction. The ϑ-distribution shows that a major part of the electrons is emitted at small angles because of the higher energy of the proton beam. Owing to this fact it is possible to detect interesting events even with the Jet Trigger only partially commissioned in the forward direction.

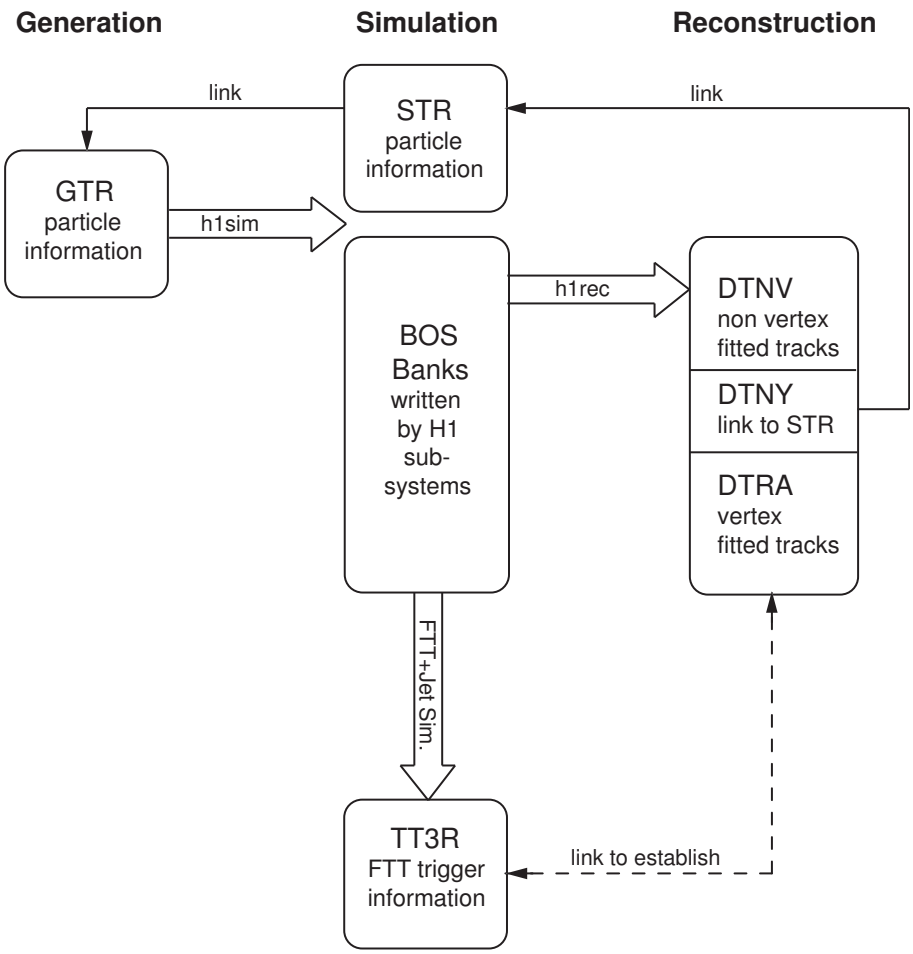

Figure 16: Displayed is the data processing of a simulated and reconstructed event. The generated information is stored in the GTR bank and is used to perform the H1 detector simulation (h1sim). h1sim creates the STR bank (containing the particle information on simulation level) and the BOS banks written by the different subsystems of the H1 experiment. The TT3R bank is generated by the FTT- and Jet Trigger Simulation in a separate step. At last the reconstruction software h1rec provides the track information in the DTNV and the DTRA bank. In order to trace back the particle relations links from the reconstructed to the simulated information (DTNY→STR) and from the simulated to the generated information (STR→GTR) are available. Furthermore, a link from the FTT to the DTNV data is established within this analysis.

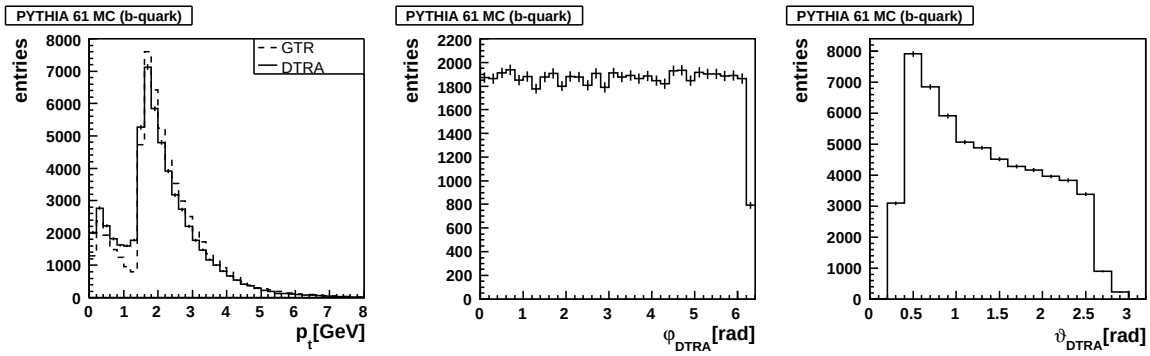

Figure 17: $p_{\perp_{DTRA/GTR}}$-, φ_{DTRA}- and ϑ_{DTRA}-distribution of the reconstructed tracks originating from generated MC electrons.

5.4.3 Track-Cluster Matching for Generated Electrons

The FTT and Jet Trigger response caused by electrons from b-decays generated in a MC simulation is investigated in this section.
To every FTT track the corresponding reconstructed and vertex fitted DTRA track is assigned. The matching of the Jet Trigger clusters to the FTT track is then carried out only for tracks originating from a generated electron. The cuts on the minimum transverse momentum of the FTT track and the minimum energy of a cluster are set to $p_{\perp_{FTT}} > 1$ GeV and $E_{JT} > 10$ counts, respectively. The correlation of the FTT- and the Jet Trigger- response is shown in Fig. 18.
The plots indicate that a cut of $\Delta\varphi \lesssim 0.3$ rad can be applied without loosing too much of the signal. A similar statement is true for the cut in $\Delta\vartheta$.
The $E_\perp/p_\perp$-distribution of matched track-cluster pairs is shown in the third plot. The cuts are set to $\Delta\varphi$=0.25 rad and $\Delta\vartheta$=0.25 rad, whilst no minimum threshold in $E_\perp/p_\perp$ is applied. The shape of the $E_\perp/p_\perp$-distribution confirms the considerations of the previous section as the peak position lies within 0.5 and 1.1.

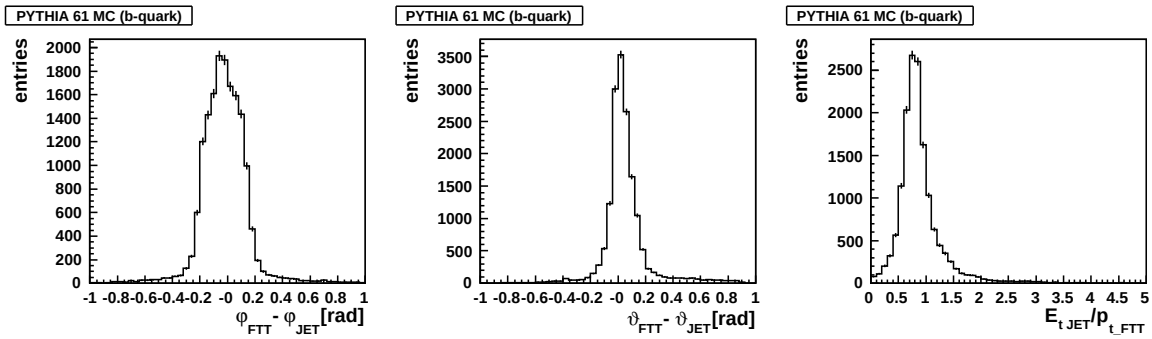

Figure 18: Spatial correlation of the FTT tracks and Jet Trigger clusters ($\Delta\varphi$- and $\Delta\vartheta$-histogram) and $E_\perp/p_\perp$-distribution obtained by the FTT - Jet Trigger matching in the b-quark MC simulation. Only the signatures of generated electrons are taken into account.

5.4.4 Efficiency in Simulated b-Quark Production Events

The efficiency of the L3 trigger depends highly on the cuts in $\Delta\varphi$, $\Delta\vartheta$ and $E_\perp/p_\perp$ as well as on the momentum of the electron. These effects will be examined in the following.
The electrons to which the efficiency determination refers to (selected electrons) have a transverse momentum of $p_{\perp_{GTR}} > 1.5$ GeV, are reconstructed in the acceptance region of 0.4 rad $< \vartheta_{\mathrm{DTRA}} <$ 0.9 rad and have been found by the reconstruction to originate from the primary vertex. The efficiency is calculated by dividing the number of triggered selected electrons by the number of generated selected electrons.
The effects of the $\Delta\varphi$- and $\Delta\vartheta$-cuts in the FTT - Jet Trigger matching on the efficiency are analysed separately. The cuts are varied in steps of 0.05 rad. The increase of the efficiency with the growing acceptance of the cuts can be seen in Fig. 19. The value of about 80% efficiency when no cuts are applied corresponds to a large extent to the combined efficiency of the first two levels of the FTT and the Jet Trigger. In the simulation the FTT achieves an efficiency of 87% and the Jet Trigger achieves an efficiency of 91%. These values are calcualted by requiring a FTT track or a Jet Trigger respectively lying in a 0.2 rad×0.2 rad $\vartheta\varphi$-window around the reconstructed track belonging to the generated electron.
In order to take the momentum dependence into account the efficiency of finding low- and high- $p_\perp$-electrons ($p_\perp \lessgtr 3$ GeV, respectively) is plotted separately. Major differences arise when applying cuts more restricting than $\Delta\varphi$=0.2 rad.
The efficiency decreases significantly for $\Delta\varphi < 0.2$ rad. The $\Delta\vartheta$-distribution shows a transition at a similar value.
For the determination of the optimal choice of the lower $E_\perp/p_\perp$-threshold, the cuts in the matching are set to $\Delta\varphi = 0.25$ rad and $\Delta\vartheta = 0.25$ rad. The $E_\perp/p_\perp$-ratio of the cluster-track-combination is computed and the lower threshold is raised in steps of 0.1. The behaviour of the efficiency plotted in Fig. 20 as function of the $E_\perp/p_\perp$-cut implies that the threshold cannot be set to a value much higher than 0.4 without a significant efficiency loss. However, a higher threshold would be needed to discriminate the electron signature reliably from the hadronic background. In the following the $E_\perp/p_\perp$-cut is set to 0.4.
The φ- and ϑ- dependence of the resulting efficiency is shown in Fig. 21. In the simulation the sensitivity of the electron trigger does not depend much on the position in space and reaches a value of about 75%.
In a next step the dependence of the efficiency on the transverse momentum of the electrons is studied. Furthermore, the cuts on the minimal transverse momentum of the FTT track and the minimal energy of a Jet Trigger cluster to be taken into account for the matching are varied. Fig. 22 and Fig. 23 show the result of these variations as function of the generated and the reconstructed momentum of the electron. In the plots on the left hand side the FTT cut is varied ($p_{\perp_{FTT}} > 1$ GeV, 1.5 GeV and 2 GeV, $E_{JT} > 10$ counts), on the right hand side the minimal Jet energy is modified ($E_{JT} > 10$, 15, 20 counts, $p_{\perp_{FTT}} > 1$ GeV). The steep increase of the efficiency at low values of the generated transverse momentum is a border effect at the acceptance limit. Apart from this effect the efficiency hardly depends on the momentum and achieves a value of about 75% at high $p_\perp$.

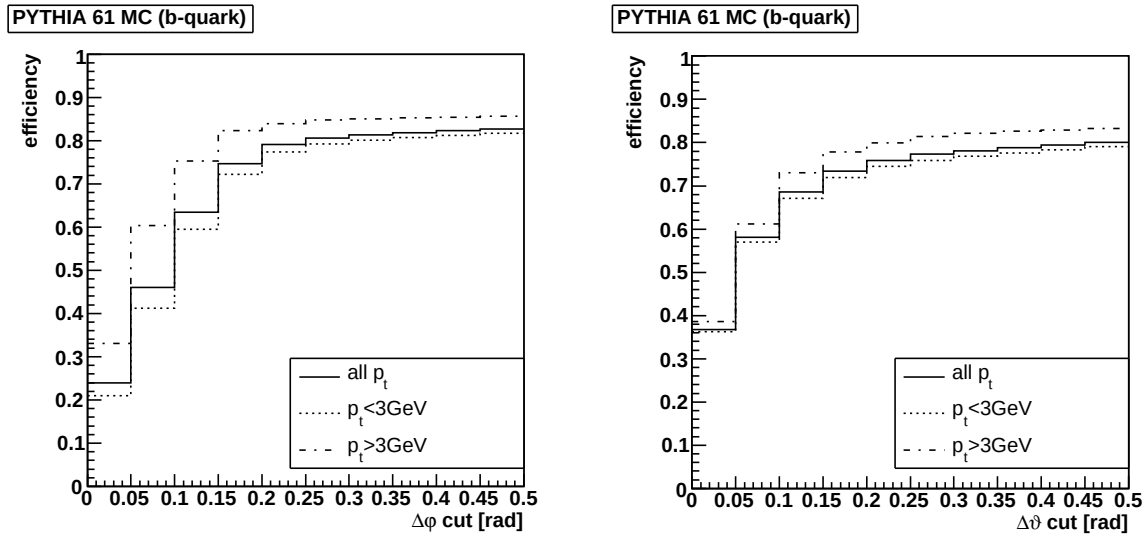

Figure 19: Efficiency of the L3 electron trigger in the b-quark MC simulation as function of the $\Delta\varphi$- and $\Delta\vartheta$-cuts. The three lines correspond to different values of the momentum of the generated electron.

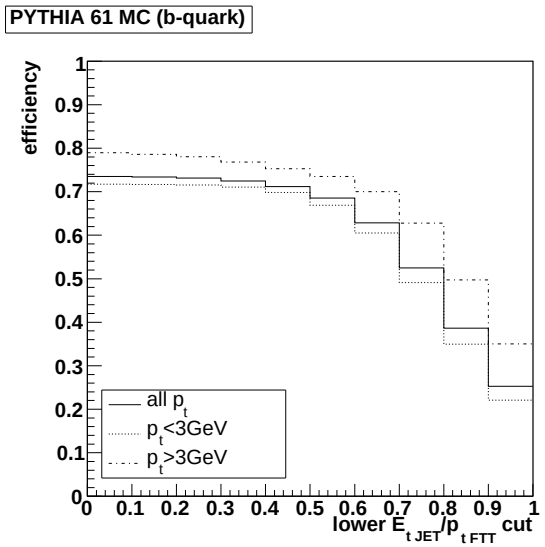

Figure 20: Efficiency of the L3 electron trigger in the b-quark MC simulation as function of the lower $E_\perp/p_\perp$ threshold. The three lines correspond to different values of the momentum of the generated electron.

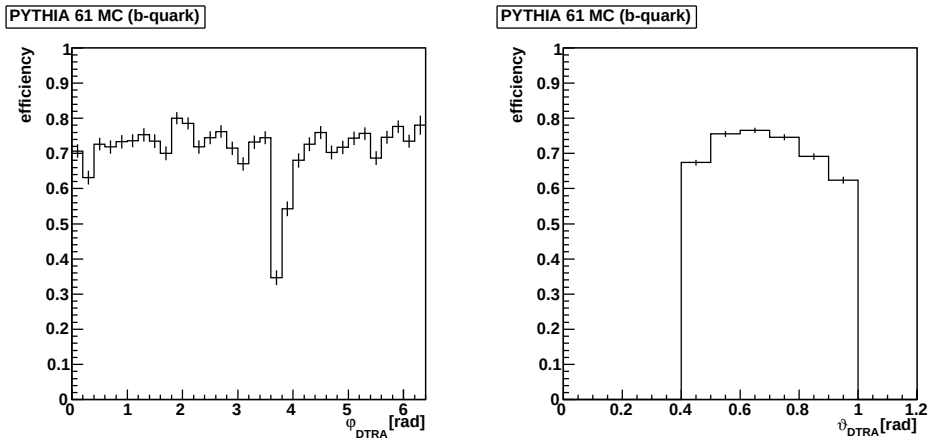

Figure 21: Efficiency of the L3 electron trigger as function of φ_{DTRA} and ϑ_{DTRA}.

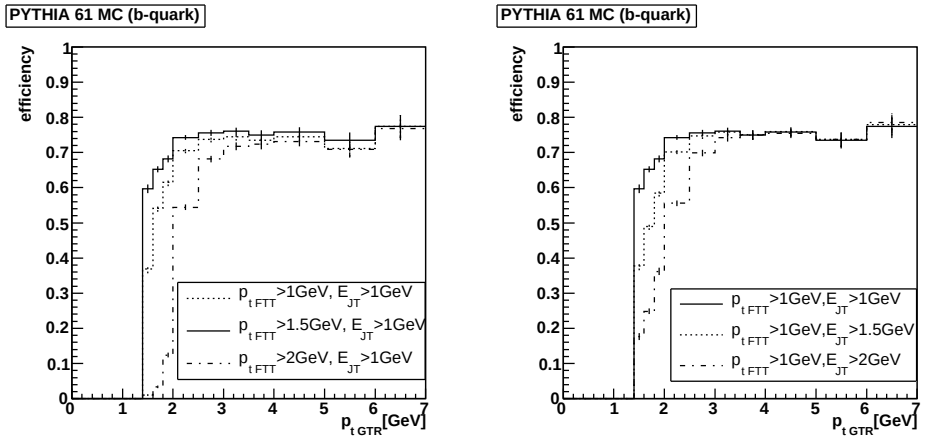

Figure 22: Efficiency of the L3 electron trigger as function of the generated momentum.

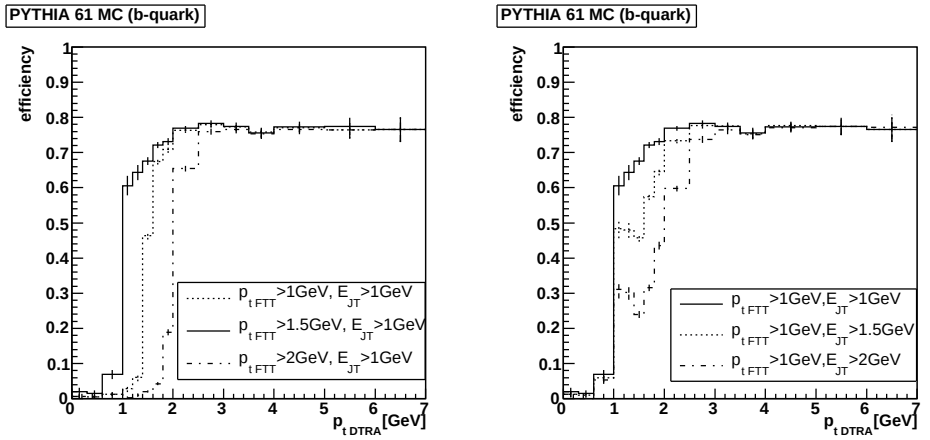

Figure 23: Efficiency of the L3 electron trigger as function of the reconstructed momentum.

5.5 Trigger Efficiency in a preselected J/Ψ → ee Sample

A sample of preselected events with a J/Ψ-resonance decaying into an e^+e^--pair is chosen to evaluate the potential of the L3 electron trigger in data taken by the real experiment. The signature of these events is suitable as it contains only two isolated leptons with a transverse momentum of 1-4 GeV which should clearly be identified by the L3 electron trigger.
The setup of the L3 electron trigger is chosen according to the results derived in the previous section. The cuts on the matching parameters are set to $p_{\perp_{FTT}} > 1$ GeV, $E_{JT} > 10$ counts, $\Delta\varphi < 0.25$ rad and $\Delta\vartheta < 0.25$ rad. The lower threshold in $E_\perp/p_\perp$ is 0.4.
The efficiency is calculated with respect to all electrons reconstructed within the acceptance region and is displayed as function of the reconstructed values of $p_{\perp_{DTRA}}$, φ_{DTRA} and ϑ_{DTRA} (Fig. 24).
The J/Ψ →ee sample contains 890 events with limited statistics. A satisfactory performance of the L3 electron trigger can be observed. All distributions show a flat shape at an efficiency level of about 75-80% that falls off only near the acceptance limit. The value of the measured efficiency corresponds to the one calculated in the MC simulation ($\sim 75\%$).

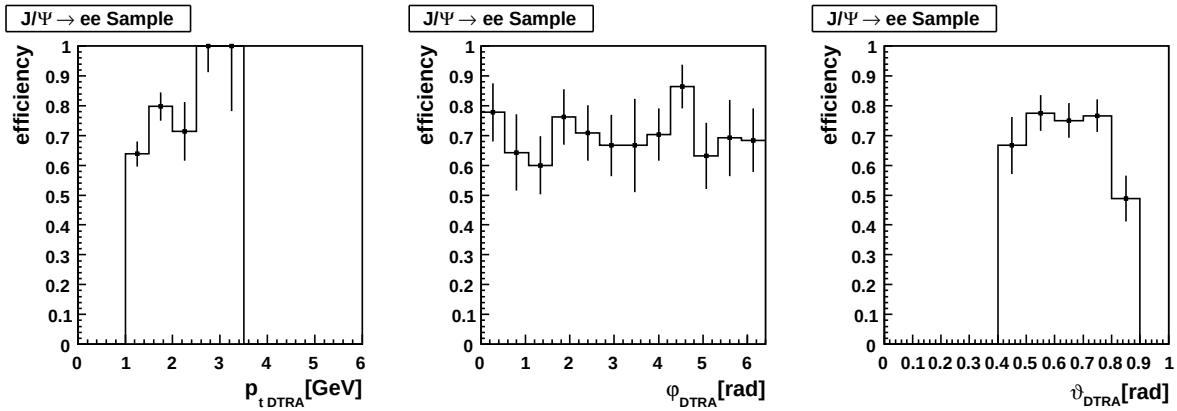

Figure 24: Efficiency of the L3 electron trigger in a preselected J/Ψ → ee sample as function of $p_{\perp_{DTRA}}$, φ_{DTRA}, ϑ_{DTRA}.

5.6 Trigger Efficiency in Data of Photoproduction Events

In this section the performance of the L3 electron trigger on a data sample of photoproduction events is discussed. The description of the event selection is followed by an efficiency comparison between data and MC.

5.6.1 Selection of the Electron Candidates

Given that a preselected b→eX sample has not been available for this study, the efficiency in data is estimated by investigating photoproduction events. The events are triggered by the L1 photoproduction subtriggers 53, 56 and 120. These subtriggers have all the same L1 condition asking for a high multiplicity event and differ on L2 in the requirements of the event topology (Table 4).
On the basis of this data a selection of the interesting physics events is performed by defining adequate criteria to identify electron candidates.
A quality flag (Q_{electron}) evaluating the probability of each reconstructed track to originate from an electron is reconstructed and written to the DTNV bank. The complex algorithm

used to determine this probability is described in [21]. The quality flag can take a value between 0 (no evidence for an electron) and 3 (high evidence). In the scope of this analysis an electron quality of 2 or 3 is required.
Furthermore, isolation criteria are applied in order to ensure the presence of a clear electron signature in the calorimeter. The energy (E_{ic}, E_{oc}) of LAr cells lying in two cones of different sizes surrounding the track is measured. The inner cone has a radius of $R^2 = (\Delta\varphi)^2 + (\Delta\vartheta)^2 = 0.03$ rad^2 corresponding to the resolution of the LAr calorimeter whereas the outer cone ($R^2 = 0.5$ rad^2) is chosen according to the spatial granularity of the Jet Trigger. In both cases the dead material corrected electromagnetic energy scale (accessible via the AE1R bank) is used. A track is defined to be isolated if at least 60% of the energy measured by the outer cone lies within the inner cone ($E_{ic}/E_{oc} > 0.6$).
In order to allow a comparison of the efficiency study in data and simulation a MC simulation of minimum bias photoproduction events is also used.
The electrons in the photoproduction MC simulation are generated with a minimal transverse momentum of $p_{\perp_{GTR}} > 1.9$ GeV. Therefore the acceptance cut of the electrons to be considered in the efficiency calculation is raised for this study to $p_{\perp_{DTRA}} > 2$ GeV.
The electron criteria together with the isolation criteria are applied in both samples (photoproduction events and simulation). The E_{ic}/p_{DTRA}-distribution of the selected electron candidates with $p_{\perp_{DTRA}} > 2$ GeV in the acceptance region is shown in Fig. 25.
A good correlation between the data sample and the minimum bias photoproduction MC simulation can be observed. The b-quark MC simulation shows a narrow peak at one whereas the peak position in the other two samples is shifted to a lower value. This shift is due to different signal to backgound ratios in the samples.
In the b-quark MC simulation most events contain an isolated electron with a transverse momentum of at least 1.5 GeV in the acceptance region. Therefore, the probability is increased that the isolated electron criteria actually identifies a true electron.
For the data sample and the minimum bias photoproduction MC simulation a FTT track above a minimum $p_\perp$ threshold is required (>1.8 GeV in data on L1, >1.9 GeV in the MC simulation). This track can originate from an electron or a hadron. A significant amount of wrongly identified electrons has to be expected when applying the discussed criteria. Fig. 25 implies that more than the half of the selected tracks are caused by background signatures.
In total, a fraction of about 10% of the electrons generated in the b-quark MC simulation fulfil the isolated electron criteria.

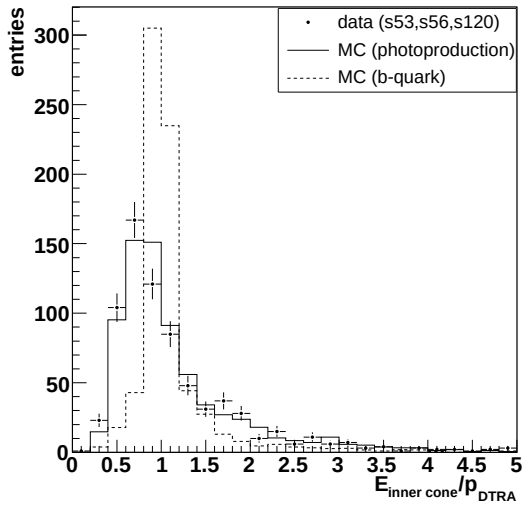

Figure 25: E_{ic}/p_{DTRA}-distribution of the particles fulfilling the isolation criteria in photoproduction data and MC simulation.

5.6.2 Efficiency in Photoproduction Events

The efficiency of the L3 electron trigger is calculated with respect to the electron candidates meeting the following criteria:

$$\mathrm{Q_{electron}} \geq 2,\ \mathrm{E_{ic}/E_{oc}} > 0.6,\ \mathrm{p_{\perp_{DTRA}}} > 2\ \mathrm{GeV},\ 0.4\ \mathrm{rad} < \vartheta < 1\ \mathrm{rad}.$$

The L3 electron setup requires an FTT track with $p_{\perp_{FTT}} > 2$ GeV and matching parameters of $\Delta\varphi$=0.25 rad, $\Delta\vartheta$=0.25 rad and $E_\perp/p_\perp > 0.4$. The results of the efficiency calculation are shown in Fig. 26, Fig. 27 and Fig. 28. The first three plots show the efficiency as function of $p_{\perp_{DTRA}}$, φ_{DTRA} and ϑ_{DTRA}. The efficiency calculation is performed for all three samples: the sample of measured photoproduction events (points), the minimum bias photoproduction MC simulation (solid line) and the b-quark MC simulation (dotted line).
The last plot is two dimensional and shows the efficiency as function of φ_{DTRA} and ϑ_{DTRA}.
The efficiency in data shows a flat behaviour as function of the transverse momentum of the electron. The variations for values of $p_\perp > 5$ GeV is due to limited statistics in this kinematic region. The level of the efficiency lies at about 65-70%.
In the φ_{DTRA}-distribution in data a loss of about 30% in efficiency can be observed in the region of 2.4 rad $< \varphi_{\mathrm{DTRA}} <$ 3.8 rad. The ϑ_{DTRA}-distribution shows an efficiency decrease for values of $\vartheta_{DTRA} > 0.8$ rad.
Outside of this region the efficiency reaches a value of about 70% as function of φ_{DTRA} and a value between 70% and 100% as function of ϑ_{DTRA}.
There is a remarkable good correlation of the efficiency in data and in the minimum bias photoproduction MC simulation. This confirms on one hand the reliability of the simulation and on the other hand the performance of the hardware implementation (apart from the spatial region discussed above).
In the b-quark MC simulation the efficiency reaches about 75-90%. This value however cannot be compared directly to efficiency in data as the signal to background ratio and the spectrum of the electrons in the two samples are too different.

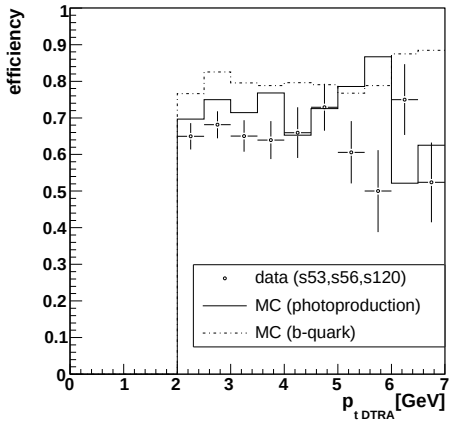

Figure 26: Efficiency of the L3 electron trigger as function of $p_{\perp_{DTRA}}$.

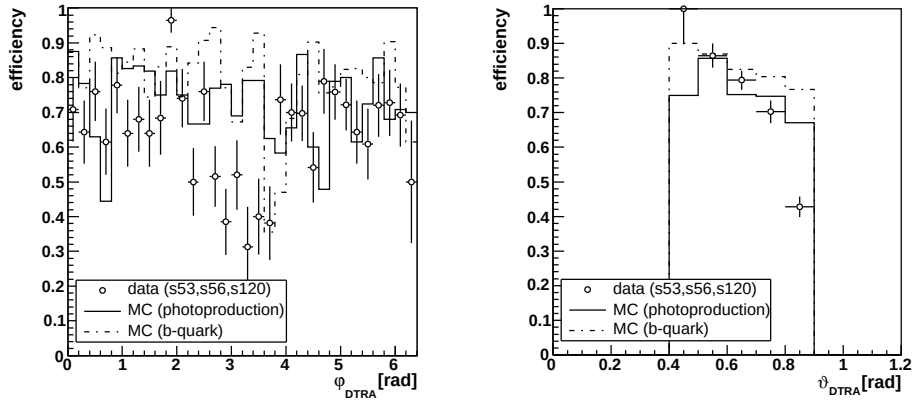

Figure 27: Efficiency of the L3 electron trigger as function of φ_{DTRA}(left) and ϑ_{DTRA}(right).

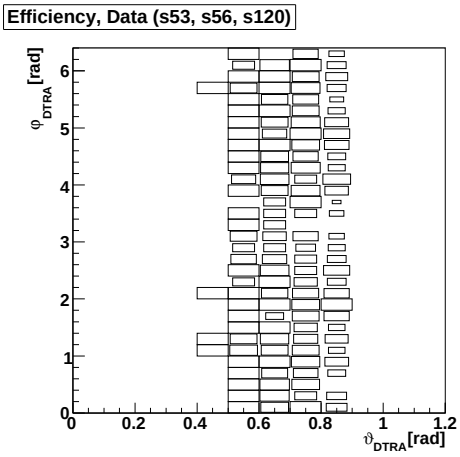

Figure 28: Efficiency of the L3 electron trigger as function of φ_{DTRA} and ϑ_{DTRA} in data.

5.7 Rate Reduction

The design of the L3 electron trigger should allow to achieve an L4 input rate of a frequency of about 1-2 Hz. The value of 1-2 Hz is determined by the allocated bandwidth on L4.
The reduction rate is calculated with regard to the rate of selected L1 and L2 conditions:

L1: The rate reduction is set in relation with the L1 rate of the subtriggers 53, 56 and 120. These subtriggers ask for a high multiplicity event in the central region of the detector. In order to study the effect of the L1 and L2 condition of the different subtriggers independently a L2 transparent run (i.e. with no events being rejected on the second trigger level) would be needed.
Since an L2 transparent run has not been taken in the considered run period, the events meeting the L1 condition of the subtriggers 53, 56 or 120 are selected from a sample triggered by the subtrigger 61. The subtrigger 61 asks for an energy deposition in the SpaCal and a track with more than 900 MeV measured by the FTT. These conditions refer to DIS events. The samples selected by the subtrigger 61 have a high purity of true ep-events.
The subtrigger 61 has a strong rejection power of background events. The higher purity in true ep-events of the sample selected by the subtrigger 61 compared to a raw sample leads to an underestimate of the signal to background rejection of the L3 electron trigger with regard to the subtrigger 53, 56 and 120 only.

L2: Three samples of events triggered by the subtriggers 53, 56 and 120, respectively are used to determine the rate rejection power of the L3 electron trigger compared to L2. The subtriggers 56 and 120 use FTT L2 conditions and a neural net for the identification of D^* events on the second trigger level whereas the subtrigger 53 uses only FTT L2 trigger elements. The details can be found in Table 4. Similar L2 conditions are intended to be used by the L3 electron trigger.
The L2 triggered samples were taken from a run when the L4 system was active. The additional L4 rejection distorts the rejection rate of the L3 trigger. It can be assumed that the events which do not pass the L4 level would have been rejected by the L3 electron trigger. Beforehand, the calculated L3 output rate is overestimated and an upper threshold for the true L4 output rate.

The rates of the L1 and the L2 trigger conditions are displayed in Table 5. In addition, the fraction of the events triggered by the subtrigger 53, 56 and 120 which are rejected on L4 is listed.

Sample	L1 Rate	L2 Rate	Rejection on L4
s53	∼600 Hz	20-80 Hz	67%
s56	∼600 Hz	5-10 Hz	30%
s120	∼600 Hz	5-10 Hz	22%

Table 5: Rates of the L1 and L2 trigger conditions (no prescale factors are applied) and rejection on L4. The fraction of events rejected on L4 is assumed to be rejected by the L3 electron trigger.

In the following three possible setups are discussed:
A single low $p_\perp$ trigger with an acceptance cut of $p_{\perp_{FTT}} > 1$ GeV, a single medium $p_\perp$ trigger with $p_{\perp_{FTT}} > 2$ GeV and a double low $p_\perp$ trigger which requires two electrons having a transverse momentum of $p_{\perp_{FTT}} > 1$ GeV.

The efficiency of these different setups is calculated from the b-quark MC simulation taking the generated electrons in the acceptance region (0.4 rad $< \vartheta <$ 0.9 rad) into account. The acceptance on the minimum transverse momentum of the generated electrons is for the low $p_\perp$ triggers at $p_{\perp_{GTR}} > 1.5$ GeV and for the medium $p_\perp$ trigger at $p_{\perp_{GTR}} > 2$ GeV. The obtained value corresponds to the exclusive L3 efficiency. The efficiency of the first two trigger levels is not taken into account as this was beyond the scope of this analysis. However, it can be assumed to be high.

5.7.1 Single Low $p_\perp$ Trigger

In Fig. 29 estimates for the efficiency and the rate reduction of the single low $p_\perp$ trigger are presented. The cut on the minimum transverse momentum measured by the FTT is $p_{\perp_{FTT}} > 1$ GeV. An event fulfils the L3 electron trigger condition if a Jet Trigger cluster is found within the acceptance window around the FTT track.
The upper two plots show the efficiency in the MC simulation versus the rate reduction obtained from data as function of the cuts in $\Delta\varphi$ and $\Delta\vartheta$. In the upper left plot the $\Delta\varphi$-cut is varied in steps of 0.05 rad (starting from 0.5 rad) whilst no cut in $\Delta\vartheta$ is applied, in the upper right plot $\Delta\vartheta$ is varied and no cut in $\Delta\varphi$ is applied. The rate reduction is displayed with respect to the L1 and the L2 conditions of the three subtriggers 53, 56, and 120.
67% of the events selected by the subtrigger 53 are rejected on L4. The L4 weighted curve corresponding to the subtrigger 53 estimates the rejection power of the L3 electron trigger in a non L4-preselected sample.
The vertical lines indicate the effect which is induced by the acceptance cut on the minimum transverse momentum of the electron. The $p_{\perp_{FTT}}$-cut leads to a rejection of 60% of the events in the L1 triggered sample and 18-26% in the L2 triggered samples.
The difference between the vertical line and the related marker corresponds to the rejection power of the actual track-cluster matching algorithm performed on L3.
The efficiency of the single low $p_\perp$ trigger decreases significantly when applying cuts more restrictive than $\Delta\varphi = 0.25$ rad and $\Delta\vartheta = 0.25$ rad. The signal to background reduction power of the cuts in $\Delta\varphi$ and $\Delta\vartheta$ are comparable. In both cases the efficiency achieves a value of about 75% for the optimum signal to background reduction.
The cuts of $\Delta\varphi = 0.25$ rad and $\Delta\vartheta = 0.25$ rad which are close to the optimum signal to background reduction are marked in the plot with filled labels.
When applying these cuts about 30% of the events triggered by the subtriggers 53 or 56 are rejected, 50% of the events triggered by the subtrigger 120 and 70% of the events only fulfilling the L1 condition. The rejection power of the cut in $\Delta\vartheta$ is slightly higher.
The bottom left plot in Fig. 29 shows the efficiency versus rate reduction as function of the minimum threshold in $E_\perp/p_\perp$.
In the bottom right plot the resulting L3 output rate is calculated starting from the maximum L1 and L2 output rate of the subtriggers 53, 56 and 120. The threshold is varied in steps of 0.1 and the cuts in $\Delta\varphi = 0.25$ rad and $\Delta\vartheta = 0.25$ rad are applied. At the optimum point in these plots, $E_\perp/p_\perp$=0.5, the trigger is 65% efficient and has a rejection power of 50-80% with respect to L2. This setup of the L3 electron trigger would lead to L4 input rates of 3-40 Hz which is higher than required.
The rate reduction with regard to L1 of 80% (corresponding to a L4 input rate of 120 Hz) indicates the need of additional trigger conditions on L2.

5.7.2 Single Medium $p_\perp$ Trigger

In the single medium $p_\perp$ trigger setup the cut on the minimum transverse momentum of a track is at $p_{\perp_{FTT}} > 2$ GeV. The momentum cut is raised in order to achieve the required L4 input rate of 1-2 Hz. The acceptance cut on the transverse momentum of the generated electron is changed accordingly to $p_{\perp_{GTR}} > 2$ GeV.
The efficiency and the rate reduction is again calculated as function of the cuts in $\Delta\varphi$, $\Delta\vartheta$ and $E_\perp/p_\perp$. The result is shown in Fig. 30. As expected the rate reduction is significantly higher compared to the setup discussed above. A maximum efficiency of about 70% is reached by the medium $p_\perp$ trigger. The optimum cut in $\Delta\vartheta$ is again at $\Delta\vartheta$=0.25 rad whereas a more restricting cut in $\Delta\varphi = 0.2$ rad can be applied. This result is consistent with the examination of the momentum dependence of the $\Delta\varphi$ and the $\Delta\vartheta$ cut plotted in Fig. 19.
In the lower plots the point of optimum signal to background rejection is at $E_\perp/p_\perp$=0.6. The efficiency has a value of 60% when applying this cut and with the L2 condition of the subtrigger 53 the maximum L3 output rate is 5 Hz.
If the L2 condition of the subtriggers 56 or 120 are chosen rates of 1-2 Hz can be reached even with a lower threshold of $E_\perp/p_\perp$=0.2.

5.7.3 Double Low $p_\perp$ Trigger

A further trigger setup which asks for the detection of two electrons is studied. The demand of finding two matched track-cluster pairs in the acceptance region lowers the rate significantly. This allows to open the cut on the minimum transverse momentum of the track which increases the sensitivity for low momentum electrons.
For the calculation of the efficiency, a b-quark MC subsample is used which contains at least two electrons with $p_{\perp_{GTR}} > 1.5$ GeV in the acceptance region.
The plots of the efficiency versus the rate reduction for this trigger setup as function of the different cuts are shown in Fig. 31. Larger cuts than $\Delta\varphi = 0.35$ rad and $\Delta\vartheta = 0.25$ rad cause no change in efficiency. These values of the cuts are applied in the lower plots.
With the L2 condition of the subtriggers 56 or 120 an L4 input rate of 1-2 Hz is reached without introducing a minimum threshold in $E_\perp/p_\perp$. In this setup an efficiency of 58% can be preserved.
If the L2 condition of the subtrigger 53 is used, the double tag electron trigger is about 50% efficient and L3 output rates of 3-10 Hz are possible.

The values of efficiency and rate reduction obtained from the calculations above have to be understand as estimates. The calculated efficiency corresponds to the exclusive L3 efficiency. When taking the efficiency of the L1 and L2 conditions into account, a lower value is expected.
The rate reduction compared to the L1 triggered sample as well as compared to the L2 triggered sample is underestimated. The L1 triggered sample has already a high purity in true ep-events due to the additional conditions of the subtrigger 61. The purity of the L2 triggered samples is increased by the rejection of background events on L4.

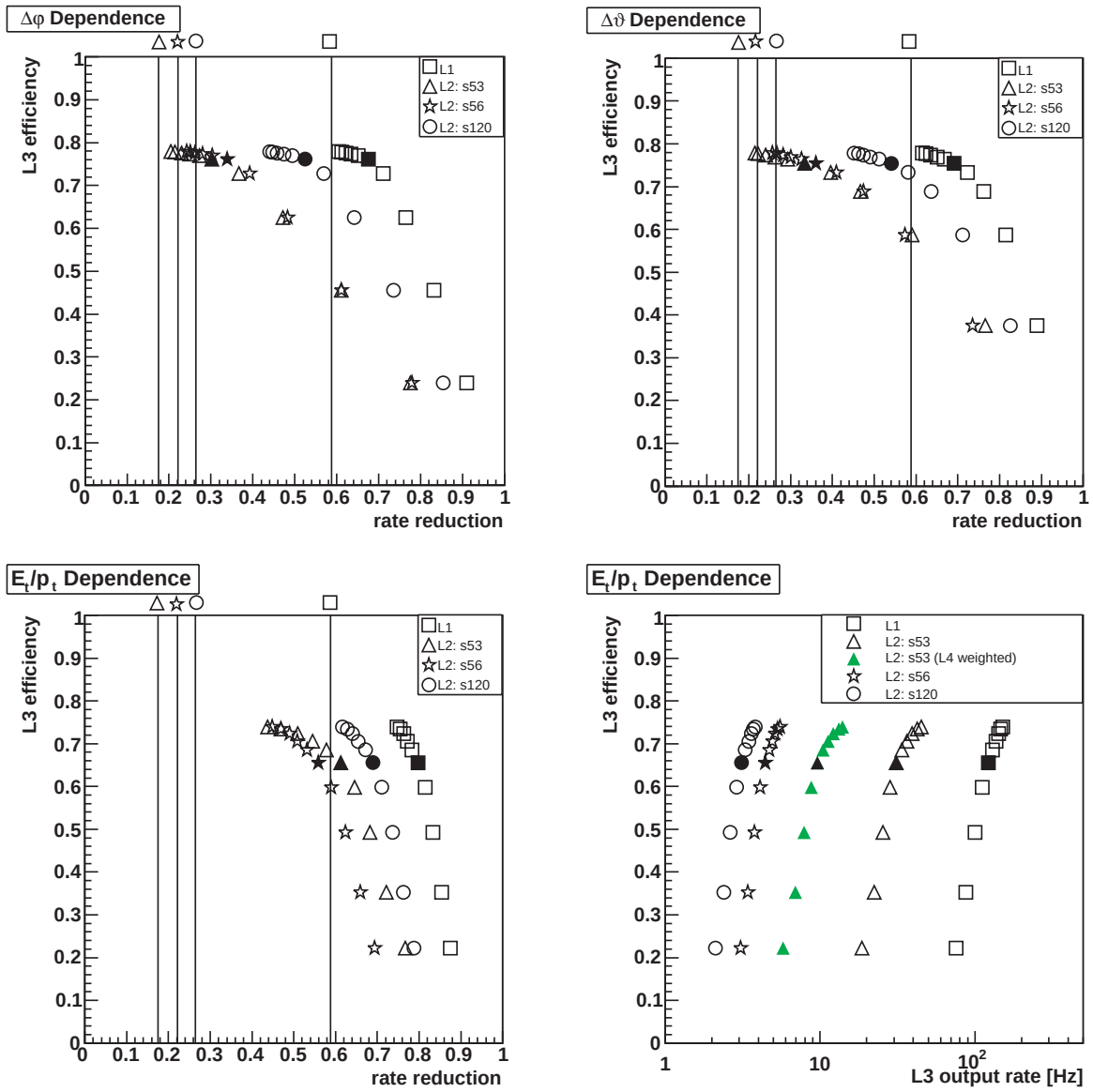

Figure 29: Efficiency of the low $p_\perp$ single electron trigger (determined in simulation) vs. the rate reduction (determined in data). The plots show the dependence of the cut in $\Delta\varphi$ (upper left), $\Delta\vartheta$ (upper right) and $E_\perp/p_\perp$ (bottom left). In the bottom right figure the efficiency is plotted vs the resulting maximum L3 output rate. The lines in the first three plots indicate the rejection rate due to the cut on the minimal transverse momentum of $p_{\perp FTT} > 1$ GeV. The filled labels mark the position of optimum signal to background reduction (upper left: $\Delta\varphi = 0.25$ rad, upper right: $\Delta\vartheta = 0.25$ rad, lower plot: $E_\perp/p_\perp$=0.5.

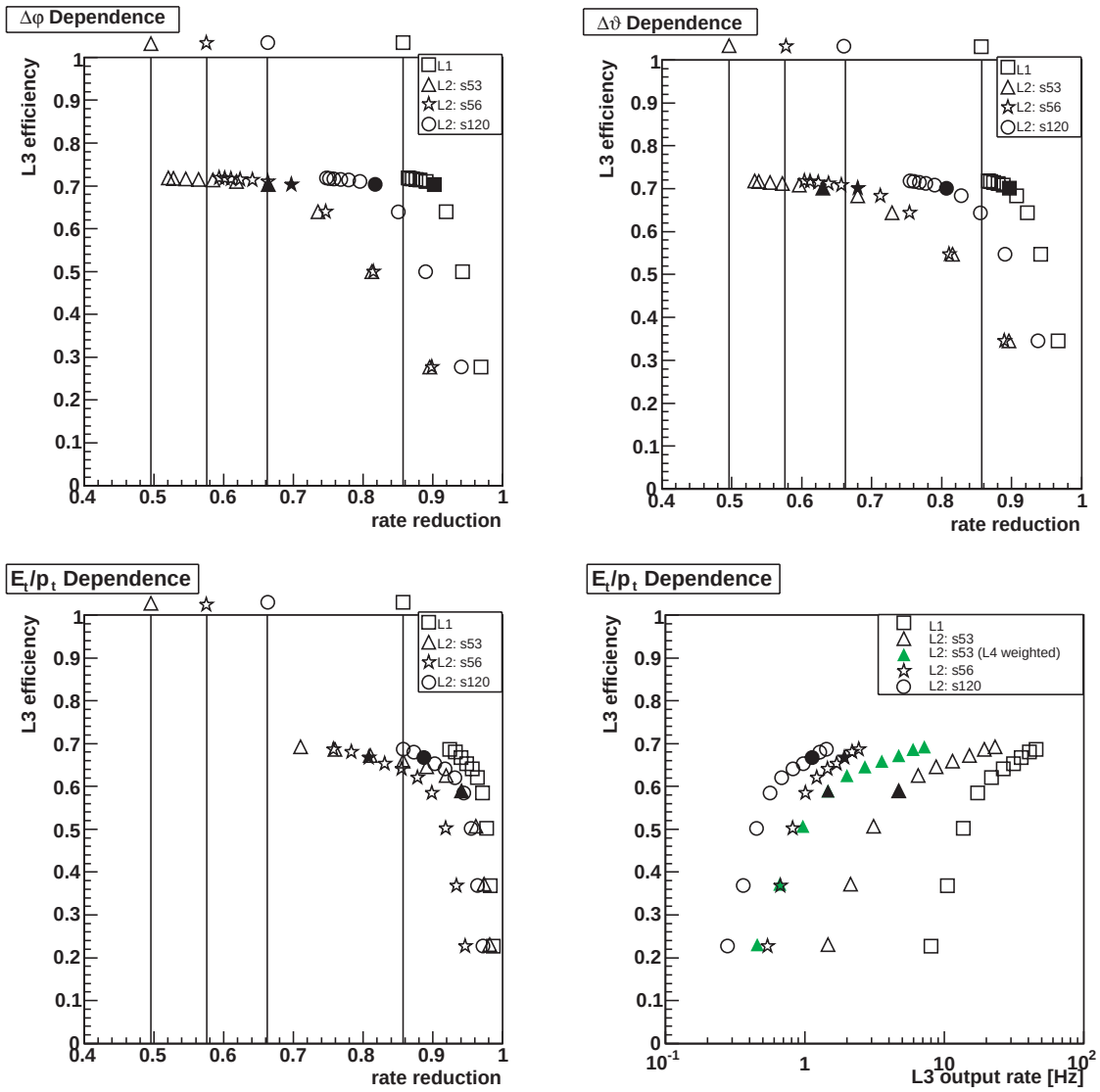

Figure 30: Efficiency of the medium $p_\perp$ single electron trigger (determined in simulation) vs. the rate reduction (determined in data). The plots show the dependence of the cut in $\Delta\varphi$ (upper left), $\Delta\vartheta$ (upper right) and $E_\perp/p_\perp$ (bottom left). In the bottom right figure the efficiency is plotted vs the resulting maximum L3 output rate. The lines in the first three plots indicate the rejection rate due to the cut on the minimal transverse momentum of $p_{\perp_{FTT}} > 2$ GeV. In the upper two plots the filled labels mark the position of optimum signal to background reduction (upper left: $\Delta\varphi = 0.2$ rad, upper right: $\Delta\vartheta = 0.25$ rad. In the lower two plots the lower thresholds chosen in the proposed trigger setup are marked: for s53: $E_\perp/p_\perp$=0.6, for s56 and 120: $E_\perp/p_\perp$=0.2.

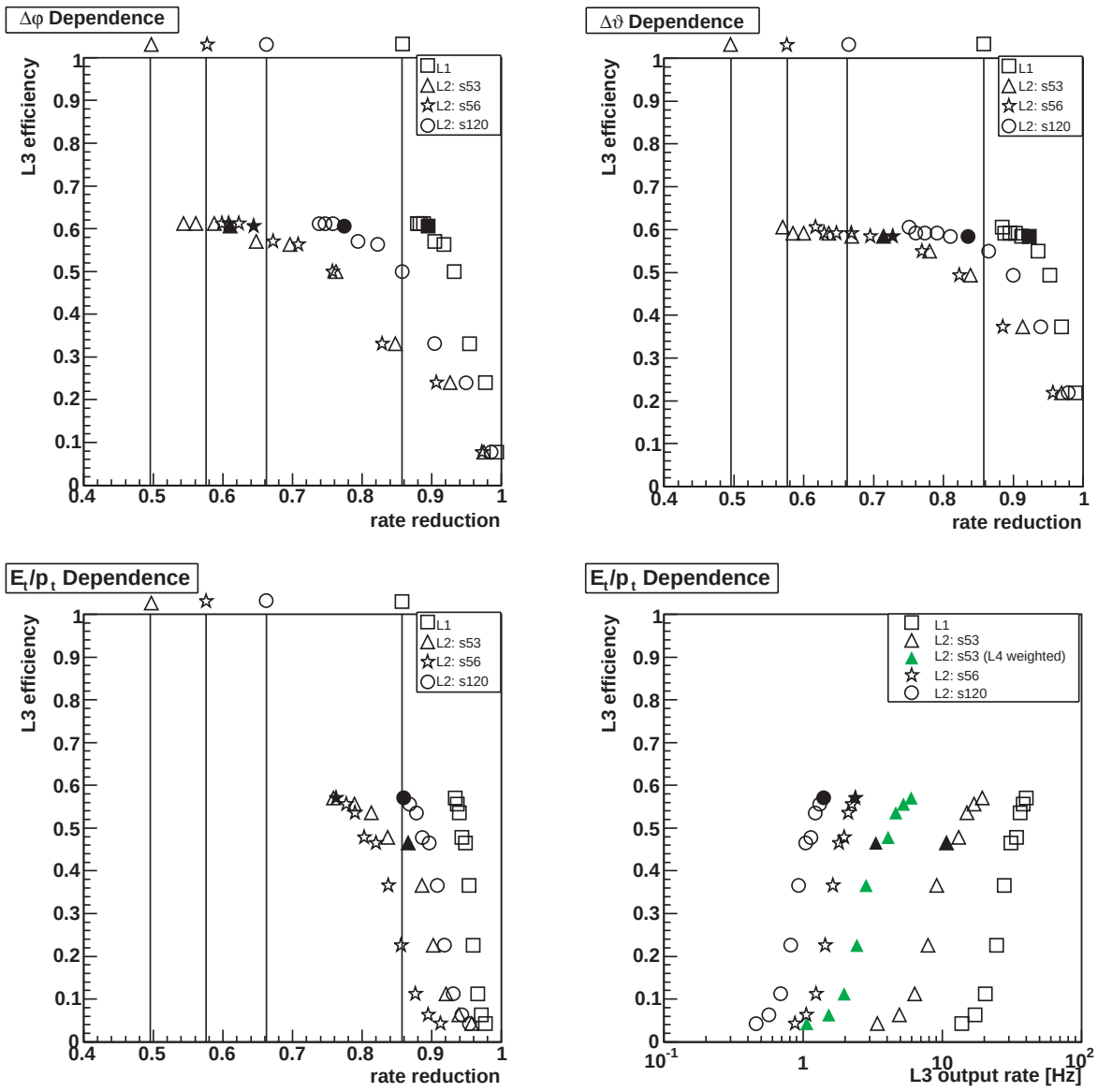

Figure 31: Efficiency of the low $p_\perp$ double electron trigger (determined in simulation) vs. the rate reduction (determined in data). The plots show the dependence of the cut in $\Delta\varphi$ (upper left), $\Delta\vartheta$ (upper right) and $E_\perp/p_\perp$ (bottom left). In the bottom right figure the efficiency is plotted vs the resulting maximum L3 output rate. The lines in the first three plots indicate the rejection rate due to the cut on the minimal transverse momentum of $p_{\perp_{FTT}} > 2$ GeV. In the upper two plots the filled labels mark the position of optimum signal to background reduction (upper left: $\Delta\varphi = 0.35$ rad, upper right: $\Delta\vartheta = 0.25$ rad. In the lower two plots the lower thresholds chosen in the proposed trigger setup are marked: for s53: $E_\perp/p_\perp$=0.3, for s56 and 120: $E_\perp/p_\perp$=0.

5.8 Proposal for Trigger Strategy

In this section a proposal for an optimum trigger setup obeying the required rate constraint is presented. With the commissioning of the Jet Trigger in the central region of the calorimeter the hardware environment for the L3 electron trigger changes. In the b-quark MC simulation 40% of the electrons are generated in the forward direction (compare Fig. 17). Thus, if the information from the whole acceptance region of the calorimeter is available, the rate is expected to increase by a factor of 2.5. The results of this study have to be revised for the new situation.
The considerations of the previous section lead to two reasonable setups for a low momentum electron trigger:

- A trigger identifying at least one electron with a momentum acceptance of $p_{\perp_{FTT}} > 2$ GeV.
- A double tag trigger which is sensitive to low momentum electrons down to $p_{\perp_{FTT}} > 1$ GeV.

The optimum setup presented in this thesis provides the running of the single electron trigger complemented for low momenta by the double tag trigger.

There are two possibilities to implement a single electron trigger. The first setup uses the L1 and L2 conditions of the subtrigger 53. In the previous section a maximum L3 output rate of 2-5 Hz was calculated. The maximum rate corresponds to the rate at the beginning of a luminosity fill. Since the rate of the subtrigger 53 decreases by a factor 4 within a single fill, the required L4 output rate of 1-2 Hz is reached. In this setup, the L3 electron trigger would have to be weighted down at the beginning of a fill, before running without prescale. An exclusive L3 efficiency of about 60% is reached.
Alternatively, the L1 and L2 conditions of the subtriggers 56 or 120 can be used. These subtriggers use a neuronal net designed to identify untagged D^* events. The response of this net to b-quark events is unclear and has to be investigated. However, a good efficiency in the events of interest can be expected as neural networks recognise general event topologies which are not much different for b-quark and c-quark production events. The L3 output rate in this setup is 1-2 Hz and the trigger is about 66% efficient.

The setup for the double tag electron trigger is also possible with the L1 and L2 conditions of the subtrigger 56 or 120 as well as of the subtrigger 53. When using the L1 and L2 conditions of the subtrigger 56 or 120, the matching can be done by applying cuts only in $\Delta\varphi$ and $\Delta\vartheta$. In this setup, the efficiency of the double tag trigger (with regard to events containing two electrons in the acceptance region) is about 60% and an L4 input rate of 1-2 Hz is reached.
A lower threshold in $E_\perp/p_\perp > 0.3$ is needed if the L1 and L2 conditions of the subtrigger 53 are used. This double tag trigger would have an efficiency of 50% and an L3 output rate of 1-10 Hz.

The optimum parameters for the setup of the presented L3 electron triggers are summarized in Table 6.
Within the scope of this analysis the inclusive L3 output rates of the different L3 electron trigger setups were calculated. These values however do not correspond to the additional bandwidth which is needed for the L3 electron trigger on L4. There is a great probability that the events containing an electron having a transverse momentum of more than ∼4 GeV are detected by the existing calorimeter triggers of H1. The $p_{\perp_{FTT}}$-, φ_{FTT}- and ϑ_{FTT}-distributions of the FTT tracks which are selected by the L3 electron trigger and the $E_{\perp_{JT}}$-,

φ_{JT}- and ϑ_{JT}-distributions of the matched Jet Trigger cluster are shown in Fig. 32. Plotted is the highest matched FTT track within the acceptance region. The setup of the single electron trigger with the L1 and L2 conditions of the subtrigger 56 are chosen in these plots. The momentum distribution of the tracks leads to the estimate that only a small fraction of the events also fulfil the requirements of an existing electron trigger. A more exact value of this factor could be obtained by investigating the online performance of the L3 electron trigger.
The optimum trigger setup presented in this thesis provides the running of a single electron trigger complemented for low momenta by the double tag trigger. The use of the L1 and L2 conditions of the L1 and L2 conditions of the subtriggers 56 or 120 is preferred. However, if the neural net would turn out not being adapted to b-quark production events, a setup with the condition of the subtrigger 53 is also possible.
The trigger decisions of the single and the double electron trigger are highly correlated which allows the combined running without causing a doubling of the L4 input rate.

	cuts	$p_{\perp_{FTT}}$	L1/L2 conditions	L3 output rate	efficiency
single tag 1	$\Delta\varphi < 0.2$ rad, $\Delta\vartheta < 0.25$ rad, $E_\perp/p_\perp > 0.5$	> 2 GeV	subtrigger 53	1-4 Hz	∼60%
single tag 2	$\Delta\varphi < 0.2$ rad, $\Delta\vartheta < 0.25$ rad, $E_\perp/p_\perp > 0.2$	> 2 GeV	subtrigger 56 or subtrigger 120 D^* (L2NN)	1-2 Hz	∼66%
double tag 1	$\Delta\varphi < 0.35$ rad, $\Delta\vartheta < 0.25$ rad, $E_\perp/p_\perp > 0.3$	> 1 GeV	subtrigger 53	1-10 Hz	∼50%
double tag 2	$\Delta\varphi < 0.35$ rad, $\Delta\vartheta < 0.25$ rad, $E_\perp/p_\perp > 0$	> 1 GeV	subtrigger 56 or subtrigger 120 D^* (L2NN)	1-4 Hz	∼60%

Table 6: Proposals for the setup of an L3 electron trigger.

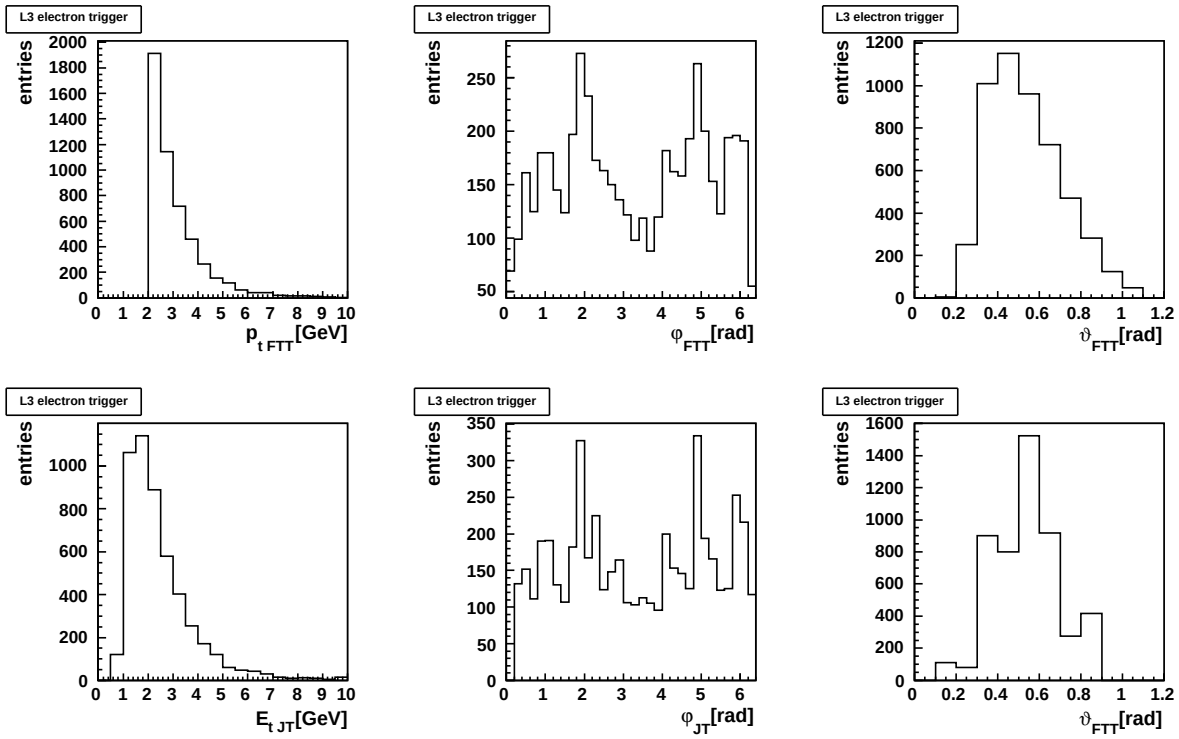

Figure 32: Upper Plots: $p_{\perp_{FTT}}$-, φ_{FTT}- ϑ_{FTT}-distribution of the highest $p_\perp$ FTT track selected by the single L3 electron trigger (using the L1 and L2 conditions of the subtrigger 56). Lower plots: $E_{\perp_{JT}}$-, φ_{JT}- ϑ_{JT}-distribution of the corresponding Jet Trigger clusters.

5.9 Hardware Implementation

The L3 electron trigger is implemented in the FTT hardware. In the current setup the L3 electron trigger runs in a transparent mode. Two bits (bit 4 and 11) on the L3 triggerbit card are available to communicate the trigger decision. Bit 11 is set if at least one track cluster pair fulfils the matching conditions, bit 4 requires the identification of at least two electron candidates.

During this first testing period the cuts in the matching are set to loose values of $p_{\perp_{FTT}} > 1$ GeV, $E_{JT} > 10$ counts, $\Delta\varphi < 0.25$ rad, $\Delta\vartheta < 0.25$ rad.

The performance of the hardware implementation of the L3 electron trigger is verified by comparing the online generated trigger elements to the ones derived in the L3 simulation software (Chapter 4). The result is plotted in Fig. 33. The response of the L3 electron trigger is consistent in data and simulation.

The figure confirms that there are no timing problems in hardware. The finding algorithm of the L3 electron trigger is able to derive a decision within the L3 latency time of 100 μs.

Shortly after the implementation of the L3 electron trigger, the work for the upgrade of the Jet Trigger in the central barrel of the calorimeter started. The Jet Trigger hardware is now completely commissioned and signals from the whole acceptance region can be processed. The final adjustment of the Jet Trigger calibration is in progress.

The performance of the L3 electron trigger with the new hardware situation has to be investigated.

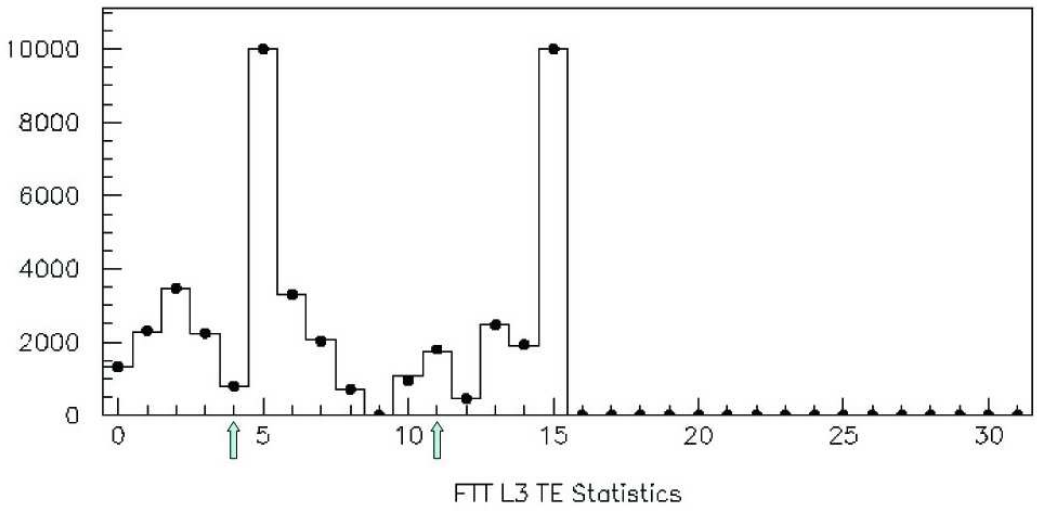

Figure 33: Comparison of the L3 trigger elements derived in the online code (points) and the FTTEMU4 simulation (solid line). The present setup of the L3 trigger elements can be found in appendix A. Bit 4 (2 electron candidates) and 11 (1 electron candidate) are generated by the L3 electron trigger.

6 Summary and Conclusions

A concept for a trigger which identifies b-quark production events using the semileptonic decay into electrons was developed within this thesis. The algorithm for this new finder is implemented on the third trigger level and uses the FTT L2 and the Jet Trigger information. The correlation of the FTT and the Jet Trigger response was investigated in measured and in simulated data. For this purpose, a software environment was elaborated which allows the combined running of the FTT and the Jet Trigger simulation.
In order to identify low energy electrons, an L3 algorithm was implemented which matches the calorimeter information of the Jet Trigger to the tracks measured by the FTT L2. Different possible setups of the L3 electron trigger were analysed by estimating the efficiency in b-quark production events generated in a MC simulation.
In addition, the hardware performance was studied with the help of a preselected $J/\Psi \rightarrow ee$ sample and a sample of photoproduction events.
The background rejection power of the L3 electron trigger was estimated compared to different L1 and L2 conditions.
As a result, a proposal for a future trigger strategy is presented. There are two possible trigger setups which lead to an estimated L3 output rate of 1-2 Hz:

- A single electron trigger which has a momentum acceptance of $p_{\perp_{FTT}} > 2$ GeV and reaches a L3 efficiency of 60-66%.

- A double tag trigger (requiring the finding of at least two electrons) which is sensitive to lower transverse momenta of $p_{\perp_{FTT}} > 1$ GeV. This trigger has an efficiency of about 50-60%.

The proposed trigger strategy provides a parallel running of the single and the double tag electron trigger. The implementation of these L3 triggers opens H1 the possibility to access the b-decay channel into electrons over a large phase space towards low momenta. Electrons with low transverse momenta down to 1 GeV can be detected.
In order to derive an optimum trigger strategy making best use of all of the first three trigger levels further investigations are needed.
Within the scope of this thesis the L3 efficiency of the electron trigger was discussed. In an advanced study, the efficiency of the discussed L1 and L2 conditions needs to be examined in data and simulation.
Furthermore, the result of this analysis have to be revised due to the new hardware situation with the Jet Trigger information available from the whole acceptance region of the calorimeter. Firstly, the Jet Trigger data received via the PQZP system has to be validated. Thereafter, the performance of the matching algorithm has to be reviewed. For this purpose the analysis software developed in this study can be used.

7 Acknowledgment

I would like to thank Prof. Eichler for making this diploma thesis possible. Special thanks go to Christoph Grab for encouraging me to carry out my diploma thesis at DESY in Hamburg. I would also like to thank all the people who contributed to the success of this dipolma thesis: Michel Sauter, Tobias Zimmermann, Benno List, Guillaume Leibenguth, Nik Berger, Ronnie Weber, Marc Del Degan, Silvan Zenklusen, Volker Michels, Daniel Beneckenstein, Andreas Jung, Bob Olivier, Katja Krüger and many others.
My very special thanks go to André Schöning for the lively discussions and his great support.

A Trigger Elements Generated on L3

Bit	Name
0	D^*
1	inelastic J/Ψ
2	D^0
3	D^0 and π_{slow}
4	double tag electron
5	D^* selection finished
6	diffractive ϱ
7	diffractive φ
8	diffractive J/Ψ
9	μ
10	diffractive φ (950-1100 MeV)
11	single tag electron
12	μ track match
13	$p_\perp\ (K) + p_\perp\ (\pi) > 1.5\ GeV$
14	$p_\perp$ (inelastic J/Ψ) > 1 GeV
15	L3 on (receiving L2 data)

Table 7: Current setup of L3 trigger elements.

List of Figures

List of Tables

References

[1] B. Wessling, Measurement of the Beauty Cross Section using the Semileptonic Decay into Electrons at HERA, Dissertation, Universität Hamburg, 2004.

[2] H1 Collaboration, Measurement of $F_2^{c\bar{c}}$ and $F_2^{b\bar{b}}$ at Low Q^2 and x using the H1 Vertex Detector at HERA, Eur. Phys. J. **C45** (2006) 23-33.

[3] H1 Collaboration, Measurement of $F_2^{c\bar{c}}$ and $F_2^{b\bar{b}}$ at High Q^2 using the H1 Vertex Detector at HERA, Eur. Phys. J. **C40** (2005) 349-359.

[4] H1 Collaboration, Measurement of Beauty Production at HERA Using Events with Muons and Jets, Eur. Phys. J. C41 (2005) 453-467.

[5] H1 Collaboration, Measurement of Charm and Beauty Photoproduction at HERA using $D^*\mu$ Correlations, Phys. Lett. B621 (2005) 56-71.

[6] ZEUS Collaboration, Measurement of open beauty production in photoproduction at HERA, Eur. Phys. J. C18 (2001) 625-637.

[7] ZEUS Collaboration, Measurement of beauty production in deep inelastic scattering at HERA, Phys. Lett. B599 (2004) 173-189.

[8] I. Abt et al., The H1 Detector at HERA, Nucl. Instrum. Meth. A 386 (1997) 310.

[9] J.H. Köhne, D. Deckert, D. Schmidt, Simulation of the PQZP System for the L2 Triggers, H1-0297-514 (H1 internal report).

[10] H1 Collaboration, Proposal to Upgrade the LAr Calorimeter Trigger: The Jet Trigger, DESY-PRC-99-02.

[11] M. zur Nedden, B.Reisert, T.Schörner , H1 Liquid Argon Trigger: Overview, Simulation and Performance, H1-04/01-592 (H1 internal report).

[12] A. Baird et al., A Fast High Resolution Track Trigger for the H1 Experiment, IEEE Trans. Nucl. Sci., 48:1276-1285, 2001.

[13] Ch. Wissing, Entwicklung eines Simulationsprogramms und Implementierung schneller Spurfitalgorithmen für den neuen H1 Driftkammertrigger, Dissertation, Universität Dortmund, 2002.

[14] D. P. C. Sankey, Proposed QT Algorithm for Fast Track Trigger, project document, H1 internal.

[15] J. Naumann, Entwicklung und Test der dritten H1-Triggerstufe, Dissertation, Universität Dortmund, 2002.

[16] A. Jung, Inbetriebnahme der dritten Stufe des schnellen Spurtriggers für das H1-Experiment, Diplomarbeit, Universität Dortmund, 2004.

[17] A. Jung, Dissertation, Universität Heidelberg, in preparation.

[18] V. Blobel, http://aleph.web.cern.ch/aleph/Aleph_Light/BosManualHome.html.

[19] T. Sjöstrand et al., High Energy Physics Event Generation with Pythia6.1, Comput. Phys. Commun. 135, 238 (2001).

[20] Jet Trigger Group.

[21] G. Schmidt, Untersuchung der diffraktiven Photoproduktion von J/Psi Mesonen im H1-Detektor bei HERA, Dissertation, Universität Hamburg, 1996.